

DETERMINATION OF THE $K_L^0 \rightarrow \pi^- \mu^+ \nu_\mu$ FORM FACTOR $\xi(q^2)$
BY MUON POLARIZATION MEASUREMENTS

Gilbert Shen

Lawrence Berkeley Laboratory
University of California
Berkeley, California

ABSTRACT

We have measured the polarization of the muon in the decay $K_L^0 \rightarrow \pi^- \mu^+ \nu_\mu$ as a function of q^2 , the four-momentum transferred to the lepton pair. The kinematic information was used to compute the polarization expected on the basis of various assumed values of the form factor $\xi(q^2)$. By comparing the interpolated curve of the polarization as a function of $\xi(q^2)$ to the experimentally measured polarization, we have determined $\xi(q^2)$ as a function of q^2 . If one parameterizes the q^2 dependence of ξ by $\xi(q^2) = \xi(0) + \Lambda q^2/m_\pi^2$, then $\xi(0) = 0.178 \pm 0.105 - 3.80 \Lambda$.

NOTICE
This report was prepared as an account of work sponsored by the United States Government. Neither the United States nor the United States Energy Research and Development Administration, nor any of their employees, nor any of their contractors, subcontractors, or their employees, make any warranty, express or implied, or assume any legal liability or responsibility for the accuracy, completeness or usefulness of any information, apparatus, product or process disclosed, or represents that its use would not infringe privately owned rights.

109

ACKNOWLEDGMENTS

This experiment was the result of a group effort. Special thanks go to the Leroy Kerth, my adviser; Alan Clark, Rolland Johnson, and R. Clive Field for their broad contributions. Other physicists who assisted were William Holley, Richard Sah, and Arthur Zingher.

Much of the physical effort involved in setting up and running this experiment was handled by our technicians. In particular, I would like to thank William Baldock for his assistance in mapping the polarimeter magnetic field; Kathleen Lucas in the mapping of the spectrometer magnets; and John Wilson for programming the PDP-9. Others were Fred Goozen, Timothy Nuzum, Gerry Schnurmacher, and Tom Weber.

This research was done under the auspices of the Atomic Energy Commission and the Lawrence Berkeley Laboratory.

DETERMINATION OF THE $K_L^0 \rightarrow \pi^- \mu^+ \nu_\mu$ FORM FACTOR $\xi(q^2)$
BY MUON POLARIZATION MEASUREMENTS

	<u>Page</u>
Abstract	
Acknowledgments	i
I. <u>Introduction</u>	1
II. <u>Theoretical Background</u>	
A. Phenomenology	3
B. Physics	5
C. Kinematics	9
D. Muon Decay Distribution	10
III. <u>Experimental Apparatus</u>	
A. Introduction	13
B. Beam	14
C. Spectrometer Magnets	16
D. Spark Chambers	17
E. Cherenkov Counters	18
F. Scintillation Counters and Hodoscopes	19
G. Range Device	20
H. Polarimeter	21
I. Trigger	25
J. Event Readout	27

IV. Method of Analysis

A. Introduction	29
B. Event Reconstruction	30
C. $K_{\mu 3}$ Event Selection	34
D. Foundations of the Polarization Measurement	36
E. Procedure	43
F. Statistics	45

V. Results

A. Results of the Analysis Procedure	48
B. Systematics	49
C. Concluding Remarks	52

Appendices

A. The Asymmetry Parameter of a Precessing Muon	54
B. Polarimeter Time Distribution Including Poisson Background	58
C. Estimated Phase Error Due to Polarimeter Inefficiency and Nonuniformity	62
D. Probabilities of the Two Possible Event Configurations	68
E. Statistical Uncertainty of the Predicted Phase	73
F. Characteristics of the Polarization Vector	77

References	81
------------	----

Figure Captions	89
-----------------	----

I. INTRODUCTION

Weak decays of the K_L^0 meson have been the subject of much investigation as a means of testing a number of predictions of current algebra and the partially conserved axial vector current hypothesis (PCAC). The semileptonic modes are particularly convenient since half of the interaction, namely the leptonic current, is familiar soil. In Section A of Chapter II we show that these semileptonic modes can be fully characterized by two form factors (i.e., functions of momentum transfer). These form factors are the interface between theory and experiment.

In Section B of Chapter II we show that a judicious choice of expressions for the form factors will isolate their physical effects. Specifically, the $\xi(q^2)$ form factor is shown to be functionally related to the muon's polarization in $K_L^0 \rightarrow \pi^- \mu^+ \nu_\mu(K_{\mu 3})$. $\xi(q^2)$ also affects the branching ratio $\Gamma(K_{\mu 3})/\Gamma(K_{e 3})$ as well as the distribution of decays over the $K_{\mu 3}$ Dalitz Plot.

There are thus three methods of determining $\xi(q^2)$. Table 1 lists past attempts at this measurement in approximate chronological order. The most recent Dalitz Plot study by Donaldson, et al.¹ is consistent with $\xi(0) = 0.0$. The polarization experiments, however, yield values of $\xi(0)$ ranging from -0.5 to -1.5. The branching ratio experiments give intermediate results, although the most recent result seems to corroborate Donaldson, et al.

This experiment is another determination of $\xi(q^2)$ from the muon's polarization, with the aim of either reconciling or confirming the differing experimental results. Our apparatus, which is detailed in Chapter III, was designed to eliminate several potential sources of systematic error that existed in previous polarization experiments. Chapter IV indicates our analysis scheme. The results of the analysis are presented in Chapter V, along with arguments to show that all systematic effects are negligible at our level of statistical precision.

II. THEORETICAL BACKGROUND

A. Phenomenology

In the current-current model of the weak interactions, the Lagrangian for a semileptonic decay is a product of the hadronic weak current and the leptonic current:

$$L = \frac{G}{\sqrt{2}} J_{\alpha}^{\text{HAD}} J_{\text{LEP}}^{\alpha} + \text{Hermitian conjugate} \quad .$$

For the particular decay mode $K_L^0 \rightarrow \pi^- \mu^+ \nu_{\mu}$, the leptonic current is known to be well represented by the V-A form

$$\langle \nu | J_{\text{LEP}}^{\alpha} | \mu \rangle = \bar{\nu}_{\mu} \gamma_{\alpha} (1 + \gamma_5) u_{\nu} \quad .$$

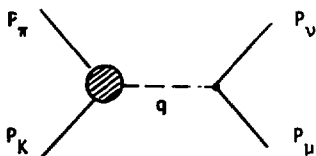
We shall ignore possible scalar and tensor couplings, which have not been exhibited in any previous experiment.² The absence of a leptonic form factor implies that the leptons interact at a point, which is a valid assumption for the range of momentum-transfers attainable in this decay.

The hadronic weak current $\langle \pi^- | J_{\alpha}^{\text{HAD}} | K_L^0 \rangle$ is complicated by the presence of form factors, indicating hadron structure at the weak vertex. In this section, we shall show that we can make some statements on the form of this current without any knowledge of the dynamics involved.

The matrix element for $K_{\mu 3}$ decay is

$$M = \frac{G}{\sqrt{2}} \langle \pi^- | J_\alpha^{\text{HAD}} | K_L^0 \rangle \bar{v}_\mu \gamma_\alpha (1 + \gamma_5) u_\nu .$$

One can represent this matrix element by a diagram in which all of the structure at the hadronic vertex is symbolized by a blob. The diagram illustrates the statement that the leptonic current acts as a probe of the hadronic vertex.



Focusing attention on the hadronic vertex, we can see that it is a function of the three 4-vectors that attach to it. Only two of them are independent by energy-momentum conservation. It is customary to choose $P_K - P_\pi$ and $P_K + P_\pi$ as our pair of basis vectors.

One might suppose that there is an additional 4-vector to consider in the spin of the exchange particle. However, if we go into the rest frame of the exchange particle, we see that: (1) the temporal component of the spin vanishes; (2) the spin component along the $K-\pi$ axis vanishes since the orbital angular momentum of the $K-\pi$ system must be perpendicular to the momenta, and (3) the azimuthal orientation of the spin about the $K-\pi$ axis has no physical import. So out of the four spin components only one degree of freedom remains, which can be taken to be J , the magnitude of the exchanged spin. Consideration of the lepton vertex shows that $J = 0$ or $J = 1$.

Apart from the kaon and pion rest masses, there is only one independent scalar that can be formed from the basis vectors. It is customary to choose $q^2 = (P_K - P_\pi)^2$, the square of the 4-momentum transferred to the lepton pair.

Since $\langle \pi^- | J_\alpha^{\text{HAD}} | K_L^0 \rangle$ is a 4-vector representing the hadronic vertex, it must be expressible as a linear combination of our basis vectors, with coefficients that at most can depend on q^2 and J . The traditional expression is

$$\langle \pi^- | J_\alpha^{\text{HAD}} | K_L^0 \rangle = f_+(q^2)(P_K + P_\pi)_\alpha + f_-(q^2)(P_K - P_\pi)_\alpha . \quad (\text{II.1})$$

The J dependence is implicitly contained in the functional forms of the form factors. This dependence will be made explicit in the next section.

B. Physics

Our quest for an understanding of the weak hadronic current in the $K_{\mu 3}$ decay has boiled down to measuring two functions of one variable.

There is nothing fundamental about the use of f_+ and f_- ; any two independent functions related to f_+ and f_- will do as well. In principle, these functions can depend on the magnitude of the exchanged spin. However, we can find a pair of form factors that will separate the dependence on the two spin states.

Let us first define

$$f(q^2) \equiv f_+(q^2) + \frac{q^2}{m_K^2 - m_\pi^2} f_-(q^2) . \quad (11.2)$$

We now observe that in the dilepton center-of-momentum (C.O.M.) frame, equation (II.1) becomes

$$\langle \pi^- | J_0^{\text{HAD}} | K_L^0 \rangle = f_+(q^2)(E_K + E_\pi) + f_-(q^2)(E_K - E_\pi) \quad (\text{II.3})$$

$$\langle \pi^- | \vec{J}_{\text{HAD}} | K_L^0 \rangle = 2\vec{p}_\pi f_+(q^2)$$

since $\vec{p}_K = \vec{p}_\pi$ in this frame. This also means that

$$q^2 = (p_K - p_\pi)^2 = (E_K - E_\pi)^2$$

and

$$m_K^2 - m_\pi^2 = (E_K^2 - \vec{p}_K^2) - (E_\pi^2 - \vec{p}_\pi^2) = E_K^2 - E_\pi^2 = (E_K + E_\pi)(E_K - E_\pi) .$$

So equation (II.3) becomes

$$\begin{aligned} \langle \pi^- | J_0^{\text{HAD}} | K_L^0 \rangle &= \frac{f_+(q^2)(E_K^2 - E_\pi^2) + f_-(q^2)(E_K - E_\pi)^2}{E_K - E_\pi} \\ &= \frac{f_+(q^2)(m_K^2 - m_\pi^2) + q^2 f_-(q^2)}{\sqrt{q^2}} \\ &= \frac{(m_K^2 - m_\pi^2)}{\sqrt{q^2}} f(q^2) . \end{aligned}$$

Since J_0^{HAD} is a scalar operator, the $f(q^2)$ form factor must describe a $J^P = 0^+$ transition. Similarly $f_+(q^2)$ must describe a $J^P = 1^-$ transition. The parity assignments are determined by the $K-\pi$ vertex.

The precision Dalitz Plot study by Donaldson, et al.,¹ suggests that the 1^- transition is dominated by the K^* ; and the 0^+ transition,

to a less certain degree, is dominated by the enhancement in the ν (1200 - 1400) region. In terms of the f and f_+ form factors, the consequences of this conclusion are that, for small values of q^2 , the q^2 dependences of these form factors are expected to be

$$f_+(q^2) \cong f_+(0)(1 + q^2/m_K^2)$$

$$f(q^2) \cong f(0)(1 + q^2/m_K^2) .$$

For polarization experiments, it is more convenient to work with yet another form factor, defined by

$$\xi(q^2) = f_-(q^2)/f_+(q^2) .$$

From equation (II.2) we see that

$$f(q^2)/f_+(q^2) = 1 + \frac{q^2}{m_K^2 - m_\pi^2} \xi(q^2)$$

so $\xi(q^2)$ determines the relative amplitude between a 0^+ and a 1^- transition.

In the dilepton C.O.M. frame, the 0^+ and 1^- transitions give opposite helicities to the muon of -1 and +1 respectively. Since both of these transitions can occur, the resulting polarization vector is not parallel to the muon's momentum. But the fact that the two transitions interfere coherently means that the polarization remains a unit vector. The modulus $|f/f_+|$ determines the polar angle of the polarization from the muon's momentum, and the complex phase of f/f_+ determines the azimuthal angle. The statements in this paragraph are treated in more detail in Appendix F.

There is thus a one-to-one relationship between the muon's polarization and the complex quantity $\xi(q^2)$. Cabibbo and Maksymowicz³ have determined this relationship to be $\hat{S} = \vec{R}/|\vec{R}|$, where

$$\vec{R} = b_1(\xi) \left[\left(\vec{P}_\mu / m_\mu \right) \left(\vec{P}_\nu \cdot \vec{P}_\mu / (E_\mu + m_\mu) - E_\nu \right) + \vec{P}_\nu \right] \\ + b_2(\xi) \left[\left(\vec{P}_\mu / m_\mu \right) \left(\vec{P}_K \cdot \vec{P}_\mu / (E_\mu + m_\mu) - E_K \right) + \vec{P}_K \right] - (Im \xi) \vec{d}$$

$$b_1(\xi) = m_K^2 + m_\mu^2 |b(q^2)|^2 + 2 \left[\text{Re } b(q^2) \right] (q_\nu \cdot q_K)$$

$$b_2(\xi) = -2(q_\nu \cdot q_K) - \left[\text{Re } b(q^2) \right] (q^2 - m_\mu^2)$$

$$b(q^2) = \frac{1}{2} \left[\xi(q^2) - 1 \right]$$

$$\vec{d} = E_K (\vec{P}_\mu \times \vec{P}_\pi) + E_\mu (\vec{P}_\pi \times \vec{P}_K) + E_\pi (\vec{P}_K \times \vec{P}_\mu) + \left[\vec{P}_\mu \cdot (\vec{P}_K \times \vec{P}_\pi) / (E_\mu + m_\mu) \right] \vec{P}_\mu$$

Time reversal invariance specifies that $\xi(q^2)$ is real, which in turn implies that the polarization lies in the decay plane when viewed from the kaon's rest frame (see reference 3). In this analysis, $\xi(q^2)$ will be assumed to be real (see reference 2, page 32).

The experimental significance of the f_+ form factor is seen by factoring it out of equation (II.1):

$$\langle \pi^- | J_\alpha^{\text{HAD}} | K_L^0 \rangle = f_+(q^2) \left[(P_K + P_\pi)_\alpha + \xi(q^2) (P_K - P_\pi)_\alpha \right]$$

Since the decay rate is proportional to $|M|^2$, the decay rate is proportional to $|f_+(q^2)|^2$.

C. Kinematics

The $K_L^0 \rightarrow \pi^- \mu^+ \nu_\mu$ decay configuration has two degrees of freedom, after ignoring those related to rotations and translations. These are commonly chosen to be E_π^* and E_μ^* , the pion and muon total energies, respectively, in the kaon's rest frame. Phase space is uniform in these two variables. The Dalitz Plot, representing the physically accessible region, is shown in Figure 1. Since $q^2 = m_K^2 + m_\pi^2 - 2m_K E_\pi^*$, the E_π^* axis also acts as a momentum transfer axis. Since the form factors are functions only of q^2 , they vary only with E_π^* and not with E_μ^* .

The Dalitz Plot population density is largest near the top and falls off roughly linearly as one moves downward. Unfortunately, the greatest sensitivity of the polarization direction to the ξ form factor occurs near the bottom of the Dalitz Plot. A measure of sensitivity is the angular change in polarization direction for a fixed change in $\xi(q^2)$. Figure 2 shows the polarization direction for $\xi = 0$ and $\xi = -1$ at various points within the Dalitz boundary.⁴ For statistical considerations, it is desirable to maximize the quantity

$$\text{Sensitivity} \times \sqrt{\text{Population Density}}$$

The point in the Dalitz Plot where this occurs is indicated by an \times in Figure 3. This is the point of maximal form factor information for an apparatus with uniform acceptance. This compares with the actual acceptance of our apparatus shown in Figure 3.

Our apparatus cannot measure the laboratory momentum of the K_L^0 . From the measured quantities, we can determine that the K_L^0 momentum

is one of two possible solutions to a quadratic equation. This quadratic ambiguity cannot be further resolved with the available information.

A characteristic of our data is that the two solutions are usually located near each other on the Dalitz Plot. This means that the two decay configurations nearly resemble each other in the K_L^0 rest frame. Roughly speaking, the two configurations are mirror images reflected through a plane perpendicular to the beam line in the K_L^0 rest frame. This reflection symmetry also applies to the muon's polarization and its sensitivity to $\xi(q^2)$. If one does not resolve the ambiguity, the resulting sensitivity becomes that of the expected polarization vector; which is the vector sum of the two possible polarization vectors, weighted by their probabilities of being the correct solution. Since the two possible polarization vectors have mirrored sensitivities, they tend to cancel each other's effectiveness. Fortunately this cancellation is not complete in our data. Due to the particular K_L^0 momentum distribution of the events accepted by our apparatus, the solution corresponding to the lower K_L^0 momentum is roughly twice as probable as the other solution. This means that about two-thirds of the potential information is destroyed by the presence of the ambiguity.

D. Muon Decay Distribution

The muon's polarization was perceived through the positron's angular distribution in the muon's decay.

In the V-A theory of the weak interactions, a muon at rest with polarization \vec{s} will emit a positron whose momentum \vec{p} has the distribution⁵

$$\frac{d^3N}{dp^3} \propto pE \left[(3 - 2x) + \frac{\vec{s} \cdot \vec{p}}{E} (1 - 2x) \right]$$

where $p = |\vec{p}|$, $E = \sqrt{p^2 + m_e^2}$, $E_{\max} = \frac{m_\mu^2 + m_e^2}{2m_\mu}$, and $x = E/E_{\max}$.
 In addition, the decay has a time distribution

$$\frac{dN}{dt} = \frac{1}{\tau} e^{-t/\tau}$$

Denoting the angle between \vec{s} and \vec{p} by θ_{sp} , the full position distribution can be written in the form

$$\frac{d^4N}{dp^3 dt} = e^{-t/\tau} \left[f(x) + g(x) \cos \theta_{sp} \right]$$

for some functions f and g of x .

If we imagine an infinitesimal positron detector located in the direction \vec{p} from the muon, then $d^4N/d^3p dt$ would be the probability density for a positron hitting the detector with momentum p at time t . If the detector has a detection efficiency $\eta(\vec{p}) = \eta(x, \theta_p)$, the probability density for actually detecting a positron is

$$r(\vec{p}, t) = \left(\frac{d^4N}{d^3p dt} \right) \eta(\vec{p})$$

If the muon is in a magnetic field \vec{B} , its polarization vector will precess about \vec{B} at the frequency $\omega_L = e/m_\mu c$:⁶

$$\frac{d\vec{s}}{dt} = \omega_L \vec{s} \times \vec{B}$$

Meanwhile, since the detector is fixed in the laboratory, \vec{p} is time

independent. The probability density for detecting a positron of momentum \vec{p} at time t then takes the form

$$r(\vec{p}, t) = e^{-t/\tau} \left[f'(\vec{p}) + g'(\vec{p}) \cos(\omega_L t + \phi_S - \phi_P) \right]$$

where ϕ_S and ϕ_P are the initial azimuthal angles of \vec{s} and \vec{p} about \vec{B} , and f' and g' are some functions of \vec{p} .

III. EXPERIMENTAL APPARATUS

A. Introduction

The apparatus was a two-armed magnetic spectrometer (see Figure 4). K_L^0 's traveling down the central axis decayed in a vacuum decay volume. The spectrometer arm containing the polarimeter was reserved for the acceptance of the secondary μ^+ , while the other arm was used for the secondary π^- from $K_L^0 \rightarrow \pi^- \mu^+ \nu_\mu$. For the momentum analyses of these secondaries, each arm contained a picture frame bending magnet bracketed by two upstream and three downstream wire spark chambers.

Since the various kaon decay modes produce charged secondaries of pions, muons, and electrons (or positrons), each spectrometer arm must be able to identify a secondary from among these possibilities. To discriminate electrons from the slower pions and muons, each arm contained a threshold Cherenkov counter. Pions and muons were distinguished from each other by an examination of their penetration into the range device or polarimeter.

The muon stopped in the polarimeter and its polarization precessed about a vertical magnetic field. The polarimeter provided information on the azimuthal angle of the initial (unprecessed) polarization vector.

An accepted event satisfied the following requirements: (1) No signal is present from either Cherenkov counter; (2) the muon track segment downstream of the magnet is parallel to the beamline to within 45 milliradians; (3) the muon must enter through the upstream end of

the polarimeter, but not exit through the rear; (4) the muon and pion tracks must pass through the horizontal hodoscopes and Chronotrons; and (5) the two tracks must be in time coincidence.

The event requirements ensure that in fact both the pion and muon tracks downstream of the magnets are roughly parallel to the kaon beam. This feature means that the spectrometer arms are approximate transverse momentum selectors. The magnets were set to select muons with an average transverse momentum of 0.176 GeV/c and pions with an average transverse momentum of 0.088 GeV/c. The low pion setting was intended to enhance the acceptance in the low pion energy region of the Dalitz Plot.

To facilitate the description of the apparatus, we introduce a right-handed coordinate frame as follows (see Figure 4):

- (1) The +y axis is "up";
- (2) The +z axis points along the beam line; and
- (3) The +x axis is in the direction $\hat{y} \times \hat{z}$.

The polarimeter lies in the positive x region.

B. Beam

The neutral beam that traveled down the axis of the apparatus was a secondary beam produced from a 0.12" x 0.25" x 4.0" copper target in the external proton beam of the Bevatron. The production angle was 3.7 degrees downward in the vertical plane (see Figure 5).

From the target, the beam first passed through a steering magnet of the proton beam channel. This magnet steered the primary beam away

from our collimation system and swept charged secondaries horizontally. The remaining neutral beam then passed through a series of collimators and vertical sweeping magnets. The vertical span of 2.4 degrees was limited by a one foot long uranium collimator (labelled "minicollimator" in Figure 5). The horizontal span of 1.0 degree was limited by a three foot uranium collimator (labelled "adjustable collimator" in Figure 5). The solid angle was thus 0.73 milliradians.

The beam then passed through a decay region consisting of a vacuum box five meters in length. The downstream exit windows which interfaced the decay region with the spectrometer arms were made from 9 ounce Dacron sailcloth covered with 5 mil Mylar to make them vacuum tight.

Since the decay region was more than 7.6 meters downstream of the target, the principle beam constituents were photons, neutrons, and K_L^0 's. A quantity of 10^{12} protons hitting the target would have generated roughly 700,000 K_L^0 's in our beam, with several hundred times as many neutrons and photons. The actual proton rate ranged from 4×10^{11} per second to 1.8×10^{12} per second.

The neutrons, photons, and K_L^0 's were routed through our apparatus via a helium-filled bag. Downstream of the magnets, the insides of the spectrometer arms were lined with 6 inches of steel, except for the range device and polarimeter. The range device was shielded by 4 inches of steel, while the polarimeter was shielded by 4 inches of lead.

Extraneous tracks in the spark chambers and hodoscopes were well within manageable limits. The multiplicity of a spark chamber gap was about 1.8 sparks per event; while each gap could accommodate at least four sparks.

In our analysis of the data, the only beam characteristics that are significant are the k_L^0 momentum spectrum (equivalently, the momentum of the primary protons) and the presence or absence of high frequency time-dependent structure. The stability of the proton momentum is characteristic of the Bevatron and is much better than our requirements. The Bevatron RF system was turned off while our data was being collected. We do not see any significant RF structure in our data.

C. Spectrometer Magnets

The spectrometer magnets were picture frame magnets (see Figure 6) with useful apertures approximately 26" high, 40" wide, and 70" long. They were skewed in the horizontal plane by 6 degrees from being squared with the beamline (see Figure 4), resulting in the outsides of the magnets being slightly upstream of the insides. This made the average trajectory more symmetric with respect to the midplane.

The magnet currents were monitored by transducers read by a digital voltmeter (DVM). The DVM values were recorded on the data tapes after each Bevatron spill.

The muon spectrometer magnet was set to a line integral of 587 kilogauss-cm, corresponding to a change in transverse momentum of 0.176 GeV/c. The pion spectrometer arm was set to a line integral of 293 kilogauss-cm, corresponding to a change in transverse momentum of 0.088 GeV/c.

D. Spark Chambers

Each spectrometer arm contained two wire spark chambers upstream of the magnet, and three more chambers on the downstream side.

Each chamber provided spark coordinates in two orthogonal directions. (See Figure 7.) One coordinate axis pointed in the y (vertical) direction, while the other lay in the horizontal plane. The exception was the middle downstream chamber, which was rotated in the chamber plane by 10 degrees in order to resolve multiple track ambiguities. The two upstream chambers were swivelled by 12 degrees to make them more nearly normal to the average track (see Figure 4).

The sensitive area of the upstream chambers was 29" high and 43" wide. The sensitive area of the downstream chambers was 38.5" high and 43" wide.

A chamber consisted of two redundant gaps, each made of two wire planes having orthogonal orientations. The 3 mil aluminum wires were spaced 1 millimeter apart. The gap was 3/8" and was filled with a gas mixture of 90% neon and 10% helium; 10% of which was bubbled through ethyl alcohol at room temperature.

When the chambers were triggered, a high voltage pulse of about 6 kilovolts was applied across each gap for 100 nanoseconds. This was followed by an 800 volt pulsed clearing field, in addition to a constant 50 volt clearing field.

Further details on the chamber construction and high-voltage supply are included in reference 7.

The spark information was read out by magnetostrictive wands, with one wand for each wire plane. The signal wires were bracketed

by fiducial wires near the ends of each wand. The peaks of the wand signal pulses were located (in time) by differentiating the wand output and using a zero-crossing discriminator. The discriminated outputs were fed into Scientific Accessories Corporation (SAC) units for digitizing the pulse times with scalers.

In the two upstream chambers of the pion spectrometer, and the frontmost chamber in the muon spectrometer, each wand was allowed six scalers in the SAC units. The remaining chambers were allotted four scalers per wand. One scaler per wand was needed for the fiducial signal.

During this experiment, the chambers performed virtually trouble-free. Our experience showed that the chambers could handle over 150 triggers per second. The actual trigger rate, however, was more typically around 40 per second.

E. Cherenkov Counters

The momenta of both secondary particles were required to exceed 550 MeV/c by the data cuts. Their maximum values were limited by the upper end of the kaon spectrum. These restrictions mean that there is a clear separation between the electron velocity spectrum and the muon and pion velocity spectra.

With the threshold set in this separation, our Cherenkov counters enabled us to discriminate electrons from pions and muons. This was achieved by filling the counters with Freon 12 at the atmospheric pressure. The Cherenkov radiation was collected by three 5" RCA4522 photomultiplier tubes, assisted by parabolic light-gathering cones⁸ and a

large concave reflector (see Figure 8). The separate phototube outputs were recorded on the data tapes as well as the OR'd signal provided to the trigger logic.

In actual operation, we had to disconnect the center phototube in the muon spectrometer because of excessive noise. This did not seem to degrade the efficiency. Also, this Cherenkov counter was not critical to the final analysis since a positron entering the polarimeter will not produce a delayed signal.

Both Cherenkov counters were determined to be better than 99% efficient when tested in a parasitic beam.⁹ An examination of data from this experiment indicates that the product of the efficiencies of the two Cherenkov counters was better than 95%. This is sufficient for our analysis, although there is no reason to doubt the earlier calibration of the Cherenkov counters.

F. Scintillation Counters and Hodoscopes

Each Cherenkov counter was sandwiched, fore and aft, between two hodoscopes that consisted of vertical staves of Pilot Y scintillator arranged in a picket fence. The upstream hodoscope contained 28 staves 1.5" wide, 0.25" thick, and 36" high. The downstream hodoscope contained 30 staves 1.56" wide, 0.50" thick, and 46" high. The phototubes alternated between the top and the bottom in adjacent staves. This pair of hodoscopes gave us prompt angular information for use in the trigger.

A hodoscope consisting of six horizontal scintillator staves was immediately behind the upstream vertical hodoscope. The four

center staves were 6" x 48" while the two outermost staves were 6.81" x 48". The horizontal hodoscope was useful in restricting the area of each spark chamber that was searched by the track reconstruction program.

Just behind the downstream vertical hodoscopes was a set of two 48" x 48" counters (Chronotron) which gave a coincident output to the trigger if the two secondaries penetrated the counters on their separate sides within about 10 nanoseconds of each other (see reference 7).

G. Range Device

The pion spectrometer was terminated by a range-measuring device (Figure 8). This device exploited the different penetrating abilities of pions and muons in order to discriminate between them.

The front section of the range device was a one meter long graphite block which degraded muons and attenuated pions. Two 3/4" thick lead sheets, one upstream and the other midway, converted electrons into photons which were in turn attenuated by the graphite.

The rear section was a multilayered sandwich of steel plates and 3/4" thick scintillators. Transverse dimensions were 48" x 48". The thickness of steel separating consecutive scintillators ranged from 1" in the front to 4" in the rear (see Figure 8). This unequal distribution of steel corresponded roughly to a 7% increase in momentum for each additional scintillator.

Figure 9 shows the distribution of uncut events in a matrix of momentum versus range (in numbers of scintillators penetrated). One can clearly see the muon ridge, which represents the empirical muon

range-momentum curve. The momenta of muons stopping in the device range from 550 MeV/c to over 1.6 GeV/c. One can also empirically obtain the muon straggle as a function of its momentum. This information was useful in determining the cuts involved in the π - μ range discrimination.

H. Polarimeter

The polarimeter (see Figure 10) had two important functions. It provided information relating to the azimuthal angle, in the horizontal plane, of the muon's polarization. It also was a range-measuring device.

As a range device, it was preceded by a graphite and lead degrader identical to the one described in the preceding section. Secondly, the polarimeter was a multilayered sandwich of aluminum plates and scintillator with transverse dimensions of 48" \times 48". However, unlike the range device of the preceding section, there was only a single aluminum plate 1.25" thick between any two consecutive scintillators. There were thirty-one scintillation counters in all, 1/2" thick, except for the front-most counter which was 3/4" thick. Figure 11 shows the empirical muon range-momentum curve for the polarimeter. The momenta of muons stopping in the polarimeter range from 600 MeV/c to 1070 MeV/c.

In order to obtain information on the muon's polarization, we exploit the parity violating property of muon decay that the higher momentum positrons are preferentially emitted in the direction of the polarization (see Section D of Chapter II). We also know that the polarization will lie approximately in the horizontal laboratory plane since

it is constrained to lie in the decay plane (see Section B of Chapter II). Because of the sandwich structure of the polarimeter, we can only determine if the positron was emitted in either the upstream ($z < 0$) or downstream ($z > 0$) hemisphere. By precessing the polarization with a vertical magnetic field, we can rotate the polarization into an orientation approximately normal to the polarimeter plates. This occurrence is marked by an extremum in the upstream-downstream positron decay asymmetry. By knowing the time it takes to achieve this orientation, one can determine the azimuthal direction in the horizontal plane of the original (unprecessed) polarization .

Of course, an extremum in the decay asymmetry is a meaningless concept for a single event. Ultimately, however, we will be dealing with large samples of events where this idea becomes sensible. This will be discussed in more detail in Chapter IV. As for discussing the polarimeter construction, we can imagine an ensemble of a typical event configuration.

The prime consideration in the polarimeter design is the precision in determining the horizontal angle of the muon's polarization. This precision increases with the decay asymmetry and the square root of the number of detected decays. This means that a compromise must be made in the amount of material that the positron is required to penetrate before it is registered in our data sample: Thicker plates will result in fewer detected decays but an increased average asymmetry (see reference 5). The amount of material thus determined is distributed into one and a half aluminum plates and 0.5 inch of scintillator; since our typical muon stops in the center of one plate and emits a

positron that reaches the second scintillator from the muon's stopping point. Requiring a coincidence from two scintillators reduces the potential random background.

Thin scintillators are desirable to minimize the fraction of muons that stop in them, instead of in the aluminum plates. Muons stopping in scintillator are immediately depolarized -- losing all polarization information.

With 0.5 inch scintillators, 1.25 inch aluminum plates, and the requirement of a two-scintillator coincidence, the polarimeter had a measured analyzing power of 0.32, and an average positron detection efficiency calculated to be about 10 percent. The fraction of muons stopping in scintillator was calculated to be 16.3 percent, which was consistent with our data.¹⁰ Of the two-scintillator coincidences, 23 percent came from muons stopping in scintillator, 59 percent came from muons stopping in aluminum, and 18 percent arose from random backgrounds.

The polarimeter was constructed with aluminum plates because aluminum is a non-ferromagnetic conductor. The non-ferromagnetic aspect removes the possibility of local field distortions. It also leaves the strength of the external field essentially unchanged (the magnetic susceptibility is 16.5×10^{-6}),¹¹ although this is not important for our analysis. The conducting property means that the polarization of a muon at rest in aluminum will behave as though it were in a vacuum.^{12,13} The semiclassical explanation for this phenomenon is that the muon is constantly exchanging electrons with the conduction band; with the average electron's dwell time being much shorter than the relaxation

time of the muon's polarization in free muonium.¹⁴ Since this relaxation time is about 3.6×10^{-11} second,¹⁵ and since we see no evidence of depolarization after several muon lifetimes, the fraction of time that an electron is bound to the muon must be a few parts per million at most.

The sandwich was wrapped in a rectangular solenoid which produced a vertical magnetic field of 98 gauss. This field was uniform to within $\pm 0.5\%$ over the useful volume. It was periodically reversed in order to eliminate some systematic effects -- the determination of the time origin in particular. The solenoid was made of hollow copper conductor, and water cooled. Instead of a sloping pitch, each turn was wound in a plane except for a dogleg in one corner to enable the current to pass from one turn to the next. The return path for the current included a straight section that ran along the vertical joint where the doglegs were. The vertical current components in the doglegs were thus cancelled by the current in the return path.

In an event, a muon enters the polarimeter and comes to rest in one of the aluminum plates. The prompt scintillation counter signals tell us in which plate the muon has stopped. At the same time, the event trigger opens a gate that allows thirty scalars to count pulses from a 50 megahertz clock. The clock never varied by more than 10 or 20 Hertz over the course of the experiment. Each scalar is associated with a different pair of adjacent counters. If a coincidence occurs in two adjacent counters after the prompt signal, the associated scalar is stopped. Ideally, the pair of counters involved is either immediately upstream or downstream of the aluminum plate that contained the stopped

muon; in that case, the delayed coincidence is assumed to be due to the emitted positron passing through the two counters. The scaler value tells us the muon's lifetime, and the location of the counter pair relative to the muon's stopping point tells us if the positron was emitted into the upstream or downstream hemisphere.

Figure 12 indicates the various delayed-signal configurations relative to the muon stopping point and their interpretations. Note that muons stopping in scintillator and decaying downstream are distinguished, and are thus eliminated from our data sample. Muons stopping in scintillator and decaying upstream are indistinguishable from upstream decays from muons stopping in aluminum. Such muons are completely depolarized, so their observed effect is to reduce the analyzing power for upstream decays to 0.28. We shall see, in the following chapter, that this does not bias our analysis.

1. Trigger

The event trigger emphasized the acceptance of $K_{\mu 3}$ events with the muon stopped in the polarimeter; while accepting other kaon decay modes, as the trigger rate permitted, in order to examine several systematic effects of the apparatus. The trigger was generated by the coincidence of signals from the Chronotron counter pair, the horizontal hodoscopes, the pair of vertical hodoscopes in the muon spectrometer, and the first two polarimeter counters at the upstream end; provided there were no signals from the Cherenkov counter in the muon spectrometer or from the penultimate polarimeter counter near the downstream

end. The timing of the trigger pulse was determined by the signal from the polarimeter's upstream counters.

The Chronotron signal made it probable that the tracks in the separate spectrometer arms originated from a single kaon decay. It also means that the secondaries were headed into the polarimeter or range device. The horizontal hodoscopes also served this latter purpose.

The pair of vertical hodoscopes in the muon spectrometer provided an approximate, but prompt, measure of the horizontal track angle. Each of the twenty-eight staves in the upstream hodoscope was tied by coincidence circuits to the six downstream staves most directly behind it. The twenty-eight coincidence outputs were then OR'd together, with the result submitted to the event trigger. Since the six downstream staves subtend a horizontal angle of about 90 milliradians, an output from the OR indicated that a track was within 45 milliradians of being parallel to the beamline -- independent of its transverse position. The apparatus thus selected muons within a restricted range of transverse momenta.

The coincidence of the first two upstream polarimeter counters ensured that the muon candidate had penetrated at least two counters into the polarimeter. The veto provision from the penultimate polarimeter counter ensured that the muon candidate did not exit through the downstream end of the polarimeter.

The veto provision from the Cherenkov counter in the muon spectrometer suppressed triggers from $K_L^0 \rightarrow \pi^- e^+ \nu_e$ decays.

The various signals that made up the event trigger were delayed by appropriate amounts so that they arrived simultaneously at the main

coincidence (i.e., their pulses overlapped in time). The leading edge of the pulse from the upstream polarimeter counters was adjusted to arrive at the main coincidence after all other leading edges but before any trailing edge. The timing of the trigger pulse was thus determined by the upstream polarimeter counters. This is relevant since the muon's lifetime is taken to be the time lapse between the event trigger and a later two-counter coincidence from the polarimeter; with a constant correction for possible differences in the amount of delay encountered by the two signals. (This constant correction can be handled by periodically reversing the polarimeter's magnetic field, as we shall see in Section E of Chapter IV). But the delay resulting from the light propagation through the four foot high scintillator plates of the polarimeter will vary from event to event. This is significant since the muon's polarization precesses at a rate of 8.3 milliradians per nanosecond. However, since the trigger pulse timing is determined by the first two polarimeter counters, the same variable delay is encountered by the trigger signal -- leaving the time lapse unaffected.

J. Event Readout

Events were read out by a standard Lawrence Berkeley Laboratory (LBL) NIDBUS¹⁶ system into a PDP-9 minicomputer. A memory buffer stored information from seven events, each packed into 240 eighteen-bit words. When the buffer was filled, it was rolled out to a disk, allowing the PDP-9 to continue collecting data. Between Bevatron spills, the buffers stored on the disk were then written onto magnetic tape.

The information saved on tape included all scintillation counters including those in the polarimeter and range device, both Cherenkov counters (including individual photomultiplier tubes), spark chamber wand signals from the SAC units, and the polarimeter scalars.

Other information saved on tape, recorded at the end of each beam spill, included the DVM values for the two spectrometer magnets and the polarimeter magnetic field.

IV. METHOD OF ANALYSIS

A. Introduction

In Section H of Chapter III we outlined how the polarimeter enabled us to measure the polarization direction in the horizontal laboratory plane. Briefly, we exploit the property of muon decay that the higher momentum positrons are preferentially emitted in the direction of the polarization. As the polarization vector precesses about the polarimeter's vertical magnetic field, the probability that the positron will be emitted into either the upstream or downstream hemisphere will rise and fall in time with it. The resulting positron time distribution for either hemisphere will be shown to satisfy the parametric form

$$R(t) = Ne^{-t/\tau}[1 + \alpha \cos(\omega t + \phi)] \quad .$$

The initial phase ϕ of the time distribution is equal to the azimuthal angle (in the horizontal plane) of the original polarization vector.

The fact that our data consist of a collection of muons with various polarizations stopping in different regions of the polarimeter modifies our interpretation of ϕ . In this case ϕ will equal the azimuthal angle of the vector sum of the polarizations over the subset of events displaying a muon decay in our polarimeter.

The quadratic ambiguity adds one final complication: Even if we knew $\xi(q^2)$ perfectly, we could not uniquely predict the polarization of any given event. Two possible solutions exist in general.

However, since it is possible to calculate the probability that the correct solution is one or the other, we can compute the expected polarization by adding the two solutions, each weighted by its probability. So "polarization" is replaced by "expected polarization" in our preceding interpretation of ϕ .

To determine $\xi(q^2)$, our approach is to make several guesses at the value of $\xi(q^2)$ and, using the Cabibbo-Maksymowicz formula, compute the expected polarization for each event. Of course, our guesses of $\xi(q^2)$ are systematically chosen to allow interpolation between guesses. The vector sum of these expected polarizations over the data sample will be the expected polarization of the data sample. Simultaneously, we accumulate the positron time distributions for the upstream and downstream hemispheres. This results in a predicted value of ϕ for each guess of $\xi(q^2)$ plus a measured value of ϕ from the time distributions. The predicted ϕ that matches the measured ϕ will correspond to the correct value of $\xi(q^2)$.

On top of the above procedures, we also separate our data into bands of expected q^2 . Presumably the q^2 dependence of $\xi(q^2)$ is smooth enough so that $\xi(q^2)$ can be considered a constant over any single band. The data from each band can be then treated in a separate analysis.

B. Event Reconstruction

The raw data tapes from the PDP-9 were analyzed off-line at the Control Data Corporation 7600 computer facility at Lawrence Berkeley Laboratory.

Since our apparatus cannot detect the neutrino or measure the kaon's momentum, our event configuration is kinematically unconstrained. Therefore in the reconstruction program, an event is characterized simply by two tracks -- one in each spectrometer arm -- that meet at a vertex in the decay region and show continuity through the spectrometer magnets. At this stage, the information from the Cherenkov counters, range device, and polarimeter was not applied. Loose cuts were applied for purposes of programming efficiency; the tighter cuts that determine our $K_{\mu 3}$ event sample were applied by a subsequent program, which will be discussed in the next section.

In the initial steps of the reconstruction process, the spark chamber scalers from the SAC units were converted into laboratory coordinates using a continuously updated table of fiducial values (approximately the average fiducial values from the previous ten events) and the spatial coordinates of the fiducials as determined by a combination of direct measurement and an analysis of tracks from data taken with the magnets turned off. If any chamber had no sparks, the event was rejected.

The horizontal hodoscopes were examined, and the event rejected if either of them showed no counter hit. If more than one counter on a side was hit, the program considered each of them in turn.

The untangling process was performed on each arm independently. Up to three possible tracks on each side could be accommodated. If more possibilities existed, the third track was replaced if the alternative had a better χ^2 fit. If either arm had no track possibilities, the event was rejected.

The x coordinates of the three downstream chambers were considered first, by taking a two dimensional view in the x-z plane. All possible pairs of horizontal track coordinates -- one from each of the two end chambers -- were considered. (If sparks occurred in both gaps of a chamber, with a horizontal separation of less than 0.4 inch, they were considered to be from the same track.) For each such pair, the ray connecting them intercepted the middle chamber. The middle chamber's gaps were then examined for sparks whose x coordinate lay within 0.4 inch of this intercept.

We now have a ray that passes within 0.4 inch of at least one spark in all three downstream chambers, and possibly a maximum of one spark in all six gaps. Multiple spark possibilities in the middle chamber were considered as separate rays. The sparks associated with each ray were then used to determine a track candidate by minimizing the χ^2 to a straight line. With $\sigma = 0.5$ inch, tracks were rejected if $\chi^2 > 3.0$.

With the candidates for tracks in the x-z plane determined, the downstream y coordinates were considered next, by taking a two dimensional view in the y-z plane. From each vertical spark coordinate in the middle chamber (sparks in the two gaps with a vertical separation of less than 0.25 inch were considered to be from the same track), two lines were drawn to the horizontal hodoscopes -- intercepting one inch above the top edge and one inch below the bottom edge of the stove that gave a signal. The intercepts of these lines with the other two chambers provided limits within which y coordinates were acceptable. If either of these chambers had no sparks within these limits, the track was

rejected. The possible spark coordinates were then fitted to a straight line by minimizing the χ^2 . With $\sigma = 0.5$ inch, the combination yielding the smallest χ^2 was saved. If no combination had a $\chi^2 < 3.0$, the track was rejected.

The track candidates in the horizontal and vertical planes were then paired together to form three dimensional tracks. If there were more than eight such combinations, the event was rejected.

The two upstream chambers were considered next. In both the x-z and y-z planes, rays passing through the various combinations of sparks from the two chambers were extended to the magnet center plane. The downstream tracks were similarly extended from the opposite direction. The downstream and upstream tracks were then matched together by requiring their intercepts at the magnet midplane to be within 2.0 inches horizontally and 1.0 inch vertically of each other. Tracks failing to match were rejected.

We now have up to three track candidates in each spectrometer arm. By extending them upstream into the decay region, tracks from the two arms were matched together by examining their point of nearest approach. This point was required to be more than 280 inches from the target (the decay region began about 300 inches from the target), and the ray from the point to the target must have an angular difference from the beam centerline of less than 60 milliradians horizontally and 20 milliradians vertically. The distance of nearest approach was required to be less than 2 inches. If more than one combination of tracks were still viable, the program opted for the combination with the smallest distance of nearest approach.

C. $K_{\mu 3}$ Event Selection

Let us assume that, for some event, our reconstruction program determines that there is one unambiguous track in each spectrometer arm. To insure that the event is $K_L^0 \rightarrow \pi^- \mu^+ \nu_\mu$ it is sufficient to show that: (1) the two tracks originate from the same decay; (2) the track in the pion spectrometer belongs to a pion; and (3) the track in the muon spectrometer belongs to a muon.

Satisfying the first requirement is straightforward. Our Chronotron counters ensure that the two tracks occurred within about 6 nanoseconds of each other. The tracks, extrapolated upstream, were required to have a nearest approach of less than 2". The separation at nearest approach has a full width at half maximum of 0.5 inch, which indicates that this cut is quite loose. The point of nearest approach, or vertex, was required to be 300" to 500" from the production target, placing it in our vacuum decay volume.

In addition, each track was required to exit the vacuum region via its thin Dacron windows. As the tracks orbited through the spectrometer magnets, they were required to miss the magnet walls.

The remaining two requirements require a knowledge of the momenta of the secondaries. This was done with an effective length approximation for the spectrometer magnets:

$$P = \frac{P_t}{\sin\beta_{out} - \sin\beta_{in}}$$

where β_{out} and β_{in} are the secondary's exit and entrance angles in the horizontal plane as measured from the axis of the magnet aperture;

and P_t is the transverse momentum change indicated in Section C of Chapter III.

To satisfy the second requirement, we utilize a Cherenkov counter and the range device. A pion signature will be the absence of a Cherenkov signal plus a range that is too short for a muon by at least 2.5 counters. Any inefficiency in these two devices is of concern since it could cause us to accept non- $K_{\mu 3}$ events. Either an electron missed by the Cherenkov counter or a muon that fell short of its expected range would produce a pion signature. The latter condition can occur if the muon scatters out through the sides of the range device. To reduce this occurrence, we project the track downstream to the z coordinate corresponding to 4 counters past the observed range. This point of the track must be at least 2" away from the sides of the range device. In addition, we require that the pion momentum be greater than 0.56 GeV/c so that the expected muon range at least reaches the first counter.

To satisfy the third requirement, we utilize a Cherenkov counter and the polarimeter, acting as a range device. A muon signature will be the absence of a Cherenkov signal plus a range expected of a muon. If D is the difference between the observed range and the expected range for a muon, then the requirement for a muon signature may be stated as

$$|D| < P_{\mu} / (0.3 \text{ GeV}/c) \quad .$$

So, for example, a 750 MeV/c muon must stop within 2.5 counters of its expected range.

We also require that

$$0.66 \text{ GeV}/c < P_{\mu} < 1.04 \text{ GeV}/c$$

corresponding to the momentum acceptance of the polarimeter. The track projected downstream to the expected muon range was also required to be at least 1" away from the sides of the polarimeter.

Inefficiencies are not a problem in the muon identification. A true muon that is misinterpreted will cause the event to be thrown out of our analysis. This may affect our statistical precision, but does not bias our answer. A true pion or positron that is incorrectly identified as a muon will not produce a delayed signal in the polarimeter, and hence will not be included in our analysis.

The requirement that a delayed signal be detected in the polarimeter, on top of the previously mentioned cuts, makes our muon identification quite tight. This in turn makes it quite likely that the secondary on the opposite side was indeed a pion. It should not be surprising that our $K_{\mu 3}$ sample seems to be very clean.

D. Foundations of the Polarization Measurement

In Section D of Chapter II it was indicated that the probability density for detecting a decay positron with momentum \vec{p} at time t , from a muon whose polarization is precessing at a frequency ω_L , has the form

$$r(\vec{p}, t) = e^{-t/\tau} \left[f'(\vec{p}) + g'(\vec{p}) \cos(\omega_L t + \phi_S - \phi_P) \right]$$

where ϕ_s and ϕ_p are the initial azimuthal angles of \vec{s} and \vec{p} about \vec{B} , and f' and g' are some functions of \vec{p} . In this experiment, \vec{B} points along the y axis and ϕ is measured in the x - z plane with $\phi = 0.0$ corresponding to the positive z axis.

Our polarimeter detects positrons in either the downstream ($p_z > 0$) or upstream ($p_z < 0$) hemispheres. This is equivalent to integrating over infinitesimal detectors covering a halfspace. For example, the probability density for detecting a positron at time t in the forward hemisphere is

$$r^+(t) = \int_{p_z > 0} d^3p r(\vec{p}, t) = \int_0^{p_{\max}} dp \int_0^\pi d\theta_p \int_{-\pi/2}^{\pi/2} d\phi_p r(\vec{p}, t)$$

We will assume that the detection efficiency of the polarimeter is left-right symmetric. Specifically, this means that

$$g'(p, \theta_p, \phi_p) = g'(p, \theta_p, -\phi_p) \quad .$$

Then

$$r^+(t) = N^+ e^{-t/\tau} \left[1 + \alpha^+ \cos(\omega_L t + \phi_s) \right]$$

where

$$N^+ \equiv \int_{p_z > 0} d^3p f'(\vec{p})$$

and

$$N^+ \alpha^+ = \int_{p_z > 0} d^3p \, g^+(\vec{p}) \cos \theta_p$$

where α^+ is the asymmetry parameter. In Appendix A it is shown that $\alpha^+ = A^+ \cos \theta_s$, where the analyzing power A^+ is independent of \hat{s} . We can therefore write

$$r^+(t) = N^+ e^{-t/\tau} \left[1 + A^+ \hat{s}(t) \cdot \hat{z} \right]$$

where

$$\hat{s}(t) \cdot \hat{z} = \cos \theta_s \cos(\omega_L t + \phi_s) \quad .$$

An identical argument for the $p_z < 0$ hemisphere gives

$$r^-(t) = N^- e^{-t/\tau} \left[1 - A^- \hat{s}(t) \cdot \hat{z} \right] \quad .$$

Up to now, we have confined our attention to a localized region of the polarimeter around a particular stopped muon. We now wish to consider a sample of data with a distribution of muons.

Given that the i^{th} muon in the sample has stopped in the polarimeter, let

$$r_i^\pm(t) = N_i^\pm e^{-t/\tau} \left[1 \pm A_i^\pm \hat{s}_i(t) \cdot \hat{z} \right]$$

be the probability density for detecting a positron in the forward or backward hemisphere at time t . Note that

$$\int_0^\infty r_i^\pm(t) < 1$$

since not all muon decays are detected.

The positron time distribution accumulated over the entire sample is:

$$R^{\pm}(t) \equiv \sum_i r_i^{\pm}(t) = \left(\sum_i N_i^{\pm} \right) e^{-t/\tau} \left\{ 1 \pm \frac{\left[\sum_i N_i^{\pm} A_i^{\pm} \hat{s}_i(t) \right] \cdot \hat{z}}{\sum_i N_i^{\pm}} \right\} .$$

If $R^{\pm}(t)$ is fitted with the parametric form

$$R^{\pm}(t) = N^{\pm} e^{-t/\tau} \left[1 \pm \alpha^{\pm} \cos(\omega t + \phi^{\pm}) \right]$$

the initial phase ϕ^{\pm} will equal the azimuthal angle of the vector

$$\vec{V}^{\pm} \equiv \sum_i N_i^{\pm} A_i^{\pm} \hat{s}_i(0) .$$

Note that the parameters in the parametric form resemble, but are not the same as previously defined variables. This is meant to be suggestive of the close relationship between corresponding variables and parameters.

With the assumption that the polarimeter is uniform and symmetric, we expect $\vec{V}^+ = \vec{V}^-$ and $\phi^+ = \phi^-$. Indeed, we can think of the two sets of data as two separate experiments measuring the same physical quantity -- ϕ . In practice, we fit $R^+(t)$ and $R^-(t)$ simultaneously, constraining $\phi = \phi^+ = \phi^-$. In this case, we expect ϕ to equal the azimuthal angle of the vector $\vec{V} = \vec{V}^+ + \vec{V}^-$.

Thus far we have ignored the possibility of a Poisson background as well as the consequences of the electronic "logic" of our polarimeter.

For each pair of adjacent polarimeter counters, the first delayed coincidence -- real or spurious -- will stop the corresponding scaler. In the off-line analysis, we examine the scalers of the counter pairs immediately upstream and downstream of the muon's stopping point. If delayed signals are indicated in both, but at different times, the scaler with the earliest time is assumed to be real, while the other scaler is ignored.

In Appendix B we show how these complications modify our parameterized time distribution into the form

$$R^{\pm}(t) = e^{-\lambda^{\pm}t} \left\{ N^{\pm} e^{-t/\tau} \left[1 \pm \alpha^{\pm} \cos(\omega t + \phi) \right] + \Lambda^{\pm} \right\} \quad (\text{IV.1})$$

Since we fit R^+ and R^- simultaneously, with $\phi = \phi^+ = \phi^-$, we have 11 parameters: λ^+ , λ^- , N^+ , N^- , τ , α^+ , α^- , ω , ϕ , Λ^+ , and Λ^- . The interpretation of these parameters is that τ is the muon lifetime, α^{\pm} is the asymmetry parameter, ω is the muon precession frequency, ϕ is the initial azimuthal phase of the muon polarization, N^{\pm} is the normalization for the real muon signals, Λ^{\pm} is the background level, and λ^{\pm} is the background rate. The interpretation of ϕ is unchanged by the random background since the background is uncorrelated with the event configuration.

For a given data sample, ϕ is a function of the $K_{\mu 3}$ form factors. If the data sample is restricted to a narrow range of q^2 , then ϕ is a function of only one parameter -- $\xi(q^2)$. This functional relationship can be uncovered by taking several *a priori* values of ξ and computing the corresponding \vec{V} . The azimuthal angle of \vec{V} is the expected value of ϕ for the assumed form factor.

One difficulty in computing \vec{V} is not being able to know precisely what N_i^\pm and A_i^\pm are for an individual event. The analyzing power A_i^\pm is expected to be quite uniform throughout the polarimeter, since it only depends on the thicknesses and homogeneity of the aluminum and scintillator plates. The normalization N_i^\pm , however, depends on the local efficiency of the scintillation counters.

But while the prescription

$$\vec{V} = \sum_i (N_i^+ A_i^+ + N_i^- A_i^-) \hat{s}_i(0)$$

looks impractical, we show in Appendix C that the sum of the polarization vectors from events with a detected positron decay is sufficiently parallel to \vec{V} . The restriction to events with detected decays is suggested by the presence of N_i^\pm in the weight of $\hat{s}_i(0)$. Two arguments are presented in Appendix C, each probably sufficient in itself but more so when compounded. Both arguments use the idea that, while detection-related biases may exist in a single event, such biases will effectively cancel themselves out in a large data sample.

The first argument is based on the property of the polarimeter that "one man's ceiling is another man's floor". A forward decay from a muon in the tenth aluminum plate and a backward decay from a muon in the twelfth plate with the same x-y coordinates involve the same scintillation counters and aluminum plates. N^+ and A^+ for the first muon should equal N^- and A^- , respectively, for the second muon. This is tantamount to saying that $N_i^+ = N_i^-$ and $A_i^+ = A_i^-$ in \vec{V} .

The second argument says that if N_i^+ and A_i^+ are uncorrelated with $\hat{s}_i(0)$, then \vec{V} is expected to be parallel to $\sum_i \hat{s}_i(0)$, whether or not the sum is over events with detected positrons. The assumption is valid if the muon's stopping point is independent of its spin. This turns out to be a good assumption, empirically. To first order, the muon momentum spectrum reflects the kaon momentum spectrum. (This also justifies the earlier assumption of left-right symmetry in the detection efficiency. The assumption may not be valid for any single event, but any such effect tends to cancel out over a large sample.)

The final complication in computing \vec{V} is the presence of the quadratic ambiguity. The i th muon has two possible polarizations -- call them \hat{s}_{iA} and \hat{s}_{iB} . In Appendix D we show that it is possible to determine the probabilities for each vector -- call them P_{iA} and P_{iB} . The expected polarization of the i th muon is therefore

$$\langle \hat{s}_i^+ \rangle = P_{iA} \hat{s}_{iA} + P_{iB} \hat{s}_{iB}$$

Also, since

$$\langle \sum_i \hat{s}_i^+ \rangle = \sum_i \langle \hat{s}_i^+ \rangle$$

the sum of $\langle \hat{s}_i^+ \rangle$ over a sample of events is the expected value of $\sum_i \hat{s}_i^+$. The statistical error for ϕ from using $\sum_i \langle \hat{s}_i^+ \rangle$ as an estimator of $\sum_i \hat{s}_i^+$ can be computed with the algorithm developed in Appendix E.

E. Procedure

To summarize the analysis scheme, we appeal to the flow diagram in Figure 13.

The raw data is filtered by cuts to yield a data sample of presumed $K_{\mu 3}$ events. The $K_{\mu 3}$ sample is further restricted to include only events that indicate a muon decay in the polarimeter. We can then distribute the events remaining into various bins of q^2 .

From this point in the analysis, each event is handled along two separate lines.

Using the polarimeter information, we bin the event in the appropriate time distribution. When the data processing is completed, the time distributions are fitted with an 11 parameter function to yield ϕ_{exp} , the measured value of the azimuthal phase angle of $\sum_i \hat{s}_i$.

Using the spectrometer information, we compute the expected polarization vector with six different values of $\xi(q^2)$: -0.5, -0.3, -0.1, 0.1, 0.3, and 0.5. Since we are working with a sample of events within a narrow range of q^2 , the q^2 variation can be ignored. Note that we want to compute the polarization of the muon in the polarimeter. To do this, we use the Cabibbo-Maksymowicz formula which gives the polarization as seen in the muon's rest frame but expressed in laboratory coordinates. Because the Lande factor $g = 2$ for the muon (the small perturbation due to quantum electrodynamic effects is negligible), we must rotate the Cabibbo-Maksymowicz result by the same angle as the muon momentum vector in passing through the spectrometer magnet. We also remark that muons do not depolarize in the process of slowing down.¹⁷

The six vectors are accumulated with the corresponding vectors from other events in the sample. When the data processing is completed, the six accumulated vectors will yield six values of $\phi_{\text{pred}}(\xi_i)$ ($i = 1, \dots, 6$), the predicted azimuthal phase angle of

$$\sum_i (P_{iA} \hat{S}_{iA} + P_{iB} \hat{S}_{iB})$$

for six *a priori* choices of $\xi(q^2)$.

If we had selected the true value of $\xi(q^2)$ in computing $\phi_{\text{pred}}(\xi)$, then we would expect that $\phi_{\text{pred}}(\xi_{\text{true}}) = \phi_{\text{exp}}$. In practice, we reverse the process. From the curve $\phi_{\text{pred}}(\xi)$, we obtain the inverted function $\xi(\phi_{\text{pred}})$. We then expect $\xi_{\text{true}} = \xi(\phi_{\text{exp}})$.

One final complication -- the determination of ϕ_{exp} presumes that we know when $t = 0.0$. However, there is some delay from the time the muon comes to rest before the scaler gates are opened. One way to get around this is to reverse the polarimeter field periodically and analyze the data from the two polarities separately in the manner outlined above. This results in two experimental phases: $\phi_{\text{exp}}^{\dagger}$ and $\phi_{\text{exp}}^{\downarrow}$. We then combine the results to get

$$\phi_{\text{exp}} = \frac{1}{2} (\phi_{\text{exp}}^{\downarrow} - \phi_{\text{exp}}^{\dagger})$$

Any phase shift caused by an incorrect zero-time will now cancel out, leaving ϕ_{exp} unaffected. In fact, the zero-time phase shift can be gotten by

$$\partial\phi = \frac{1}{2} (\phi_{\text{exp}}^{\dagger} + \phi_{\text{exp}}^{\downarrow})$$

F. Statistics

The most important contribution to the statistical error of ξ is, of course, the error in measuring ϕ from the time distributions. In fitting for ϕ with the parametric form

$$R(t) = Ne^{-t/\tau} [1 + \alpha \cos(\omega t + \phi)]$$

it turns out that ϕ is highly correlated with ω , but essentially uncorrelated with all other parameters. (This is also true in the expanded parametric form which provides for a Poisson background and the simultaneous fitting of the upstream and downstream distributions.)

If there are $M \equiv \int_{t_1}^{t_2} R(t)dt$ detected positrons in the data sample (where the scaler gate is open from t_1 to t_2) and if ω is known precisely, then the expected error in ϕ is

$$\sigma_{\phi} = \frac{\sqrt{2}}{\alpha \sqrt{M}} .$$

But, if ω is regarded as another parameter, the expected error in ϕ becomes

$$\sigma_{\phi} = \frac{\sqrt{2}}{\alpha \sqrt{M}} \cdot \frac{1}{\sqrt{1 - \rho^2}}$$

where ρ is the correlation coefficient between ϕ and ω . With $\rho \cong 1/\sqrt{2}$ in our data, our error in ϕ would increase by 41%.

It is impractical for us to independently measure ω since the error in fitting the combined data (all q^2 bands lumped together) for ω is comparable to the reproducibility of a conventional flip coil of

about 0.2%. Moreover, there are variations with position of the polarimeter field strength of the order $\pm 0.5\%$, which would necessitate a cumbersome field map as well as open the door to systematic uncertainties.

When the data is divided according to q^2 , however, some of the bands may contain only a small fraction of the events. In this case, it will pay to fix the frequency at the value obtained from the lumped data sample, with its correspondingly smaller error. For each band of q^2 , the expected error in ϕ will then be given by

$$\sigma_{\phi}^2 = \sigma_1^2 + \rho^2 \sigma_2^2$$

where σ_1 is the error in ϕ if ω were known exactly and σ_2 is the error in ϕ in the lumped data sample.

An additional, relatively minor, contribution to the statistical error in ξ comes from the uncertainty in the predicted phase caused by the quadratic ambiguity. This error is added in quadrature to the preceding contributions.

The situation here is analogous to coin tossing. If the probability of tossing a head or tail is p or q respectively, then in N tosses we expect Np heads with an error of \sqrt{Npq} . In predicting ϕ , the number of heads in N tosses becomes the vector sum of N polarization vectors, which p and q are replaced by the probabilities of the two ambiguous solutions. Just as each permutation of heads and tails among the N coin tosses has a calculable probability, each permutation of "slow K_L^0 " and "fast K_L^0 " polarizations in the N vector sum has a calculable probability. The algorithm for computing this binomial-like error is detailed in Appendix E.

For the phase analysis of this experiment, the data were in the form of two time distributions. The time dimension was quantized into 20 nanosecond bins by the 50 Megahertz clock. For convenience, we further consolidated the data into 80 nanosecond time bins. A Monte Carlo study of the statistical precision of the phase as a function of the time binning showed (see Figure 14) that there is no loss of precision from this consolidation. (Note that 80 nanoseconds is $0.036 \tau_{\mu}$ and corresponds to an angular rotation by the polarization of 39 degrees.) Together, the two distributions contained 148 time bins which were used to fit the 11 parameter function of equation (IV.1).

V. RESULTS

A. Results of the Analysis Procedure

We collected a total of 19 million triggers for our raw data. In about 75 per cent of the triggers, tracks were reconstructible in both spectrometer arms. After imposing the vertex requirements, about 63 per cent of the triggers remained as reconstructed events. In about 35 per cent of these events, the two secondary tracks were identified as a μ^+ and a π^- . After applying further $K_{\mu 3}$ cuts (mainly that the secondaries terminate in the range device or polarimeter), and requiring an apparent muon decay in the polarimeter, about 350,000 events remain, representing 1.8 per cent of the triggers. Further cuts, mainly the limits on the secondaries' momenta, reduce the sample to the final total of 207,260 -- 110,648 events with the polarimeter magnetic field pointing in the -y direction, and 96,612 events with the field in the +y direction.

Figures 15a through 15d show the time distributions for the upstream and downstream decays in two polarities of the polarimeter field. The results of the parameterized fits are presented in Table II. We note that the asymmetry is about 0.32.

The result of separating the data into bands of q^2 and fixing the precession frequency is presented in Table III. The curves of ϕ_{pred} versus ξ for the various q^2 bands are shown in Figure 16.

This gives, finally, the results for $\xi(q^2)$ (where the q^2 value is the average q^2 for the events in each band), which are presented in Table IV and Figure 17. Figure 18 shows our data superposed on the results of Donaldson, et al., which is indicated by the solid line.

If one parameterizes the q^2 dependence of ξ by

$$\xi(q^2) = \xi(0) + \Lambda q^2/m_\pi^2$$

then one gets

$$\xi(0) = 0.51 \pm 0.55$$

$$\Lambda = -0.09 \pm 0.14$$

with a correlation of -0.981. The regression line for $\xi(0)$ is given by

$$\xi(0) = 0.178 \pm 0.105 - 3.80 \Lambda \quad .$$

In particular, if $\Lambda = 0$, $\xi(0) = 0.178 \pm 0.105$.

B. Systematics

The results presented in Section A depend on the correctness of several parameters that are assumed in our analysis. To see what effect it would have on ξ if any of these parameters were incorrect, we have measured the sensitivity of our results to each of these parameters by varying them one at a time and repeating the analysis.

The results of this procedure are summarized in Table V. The statistical errors from Section A are shown for comparison. We see that

the effects are negligible (less than 10% of the statistical error). All of the parameter shifts indicated are larger than any actual shift is expected to be. The magnets can be calibrated to better than 0.1% by using the $K_L^0 \rightarrow \pi^+ \pi^-$ events in our data with the constraints imposed by the target position and the π - π invariant mass. The K_L^0 momentum spectrum, used in computing the relative weights of the two ambiguous solutions, was obtained by examining a sample of 120,000 $K_L^0 \rightarrow \pi^+ \pi^-$ events from a previous run with the same spectrometer. A skewing error will bias one solution over the other. Two independently written Monte Carlo programs produced the identical spectrum. A skewing error of as much as 1.0%/GeV is unlikely.

Radiative corrections are also negligible. Ginsberg and Smith¹⁸ have calculated that the percentage change in the transverse component of the polarization is less than 0.25% in the region of the Dalitz Plot populated by our data. Secondly, the quadratic ambiguity reduces our sensitivity to the radiative corrections by roughly a factor of 1/3 for the same reason that it reduces our sensitivity to ξ . This reduces the maximum expected angular shift to less than 1 milliradian, which is negligible.

Finally, we consider the possibility of contamination of the $K_{\mu 3}$ sample by other event types. Only contaminations with real muons entering the polarimeter will hurt us -- and then only if the muons are polarized. This is possible if a π^+ decays in flight on the polarimeter side. We discuss below the various possibilities.

1. $K_L^0 \rightarrow \pi^+ \pi^-$

The number of $K_L^0 \rightarrow \pi^+ \pi^-$ decays that we see is about 1% of the number of $K_{\mu 3}$ events. The fraction of $K_L^0 \rightarrow \pi^+ \pi^-$ decays that decay in flight and pass the muon range cut is less than 10%. Hence any effect will be below the 1 milliradian level.

2. $K_L^0 \rightarrow \pi^+ \pi^- \pi^0$

The $K_L^0 \rightarrow \pi^+ \pi^- \pi^0$ mode is suppressed by the relatively high transverse momentum requirement of the muon spectrometer. The maximum transverse momentum in a $K_L^0 \rightarrow \pi^+ \pi^- \pi^0$ decay is 0.13 GeV/c. Figure 19 shows the $(p_0')^2$ distribution from our data. p_0' is the K_L^0 momentum in the center of momentum frame of the two charged secondaries, under the assumption that the event is $K_L^0 \rightarrow \pi^+ \pi^- \pi^0$. The presence of the $K_L^0 \rightarrow \pi^+ \pi^- \pi^0$ events in our data would appear as a narrow structure near $(p_0')^2 = 0.0$, tailing off exponentially on the positive side. For illustration purposes only, the inset of Figure 19 shows the equivalent plot for the experiment of Chien, et al.¹⁹ No such structure is detectable in our data.

3. $K_{\mu 3}$ with Reversed Charges

In this case, the muon must be mistaken for a pion by the range device, most likely as a result of scattering out through the sides. If the range device were totally efficient, these events would appear to have muons in both spectrometer arms. So we can take all events in our data which are interpreted as having muons in both arms, and combine

them with our $K_{\mu 3}$ sample. This would occur if our range device always misidentified a muon as a pion. We then repeat our analysis and observe any shift in ξ . If we now (conservatively) estimate the efficiency of the range device at 90%, the expected shift will be 10% of this measured shift.

4. K_{e3}

In this case, the electron is missed by the Cherenkov counter. Following the lead of the previous paragraph, we consider events interpreted as having a muon in the polarimeter with an electron on the other side. We combine these events with our $K_{\mu 3}$ sample and observe any shift in ξ . Since we can show from our data that the Cherenkov counter is at least 95% efficient, we take 5% of this shift as an upper limit.

The results of the procedures outlined in Subsections 3 and 4 above are shown in Table VI. We see that the implied corrections to ξ are small compared to the statistical error. Note that these are to be considered as upper limits.

C. Concluding Remarks

We would like to emphasize the lack of systematic effects in our analysis. We require no Monte Carlo except to get the K_L^0 momentum spectrum. Our results do not depend on the $K_{\mu 3}$ cuts -- the important consideration is that the time distributions and the predicted phases are derived from the same data sample. We are not sensitive to dead spots or counter inefficiencies in the polarimeter since the stopping point

of a muon is largely uncorrelated with its spin. (We might remark here that if a positron emitted upstream were mistaken for a downstream emission because of counter inefficiencies, our asymmetry would be degraded but no bias in the phase results.)

We can also show that the polarimeter does not have to have a very uniform magnetic field. Our analysis allows the frequency to vary as a parameter, and the resulting value represents the average frequency over that particular data sample. When events with a higher-than-average frequency are combined with those having a lower-than-average frequency, the resultant vector precesses at the mean frequency. The apparent depolarization is negligible.

APPENDIX A

The Asymmetry Parameter of a Precessing Muon

We show here that the asymmetry parameter for a muon precessing in our polarimeter is proportional to the length of the spin projection on the precession plane.

In a right-handed coordinate system xyz , let the y axis represent the polar axis as well as the axis of precession, and let the azimuthal angle be measured from the z axis. In our polarimeter, the z axis is perpendicular to the aluminum plates. θ_μ and ϕ_μ are the instantaneous polar and azimuthal angles, respectively, of the polarization vector. Since the muon precesses, $\phi_\mu = \omega t + \phi_0$, where ϕ_0 is the initial muon azimuthal phase.

We now imagine that there is an infinitesimal positron detector in a direction $\Omega = (\theta, \phi)$ from the muon position, covering a solid angle $d^2\Omega$. Furthermore, it is sensitive only to positrons of momentum x within a momentum bite of dx , where the momentum x is in units of the maximum positron momentum. The detection efficiency is $\eta(\theta, \phi, x)$.

Given a decaying muon, then, the probability that the positron will be detected is (see Reference 5)

$$\begin{aligned} d^3N &= \frac{1}{2\pi} x^2 \left[(3 - 2x) - (1 - 2x)\cos\theta_{\mu d} \right] \eta(\theta, \phi, x) dx d^2\Omega \\ &= \left[f(x) + g(x)\cos\theta_{\mu d} \right] \eta(\theta, \phi, x) dx d^2\Omega \end{aligned}$$

where $\theta_{\mu d}$ is the angle between the polarization vector and the direction of the detector; and $f(x)$ and $g(x)$ are defined by the above equation.

But

$$\cos\theta_{\mu d} = \cos\theta\cos\theta_{\mu} + \sin\theta\sin\theta_{\mu} \left[\sin\phi\sin(\omega t + \phi_0) + \cos\phi\cos(\omega t + \phi_0) \right]$$

so that

$$\left(\frac{d^3N}{dx d^2\Omega} \right) = \eta \left[f + g \cos\theta\cos\theta_{\mu} \right] + \eta g \sin\theta\sin\theta_{\mu} \sin\phi\sin(\omega t + \phi_0) + \eta g \sin\theta\sin\theta_{\mu} \cos\phi\cos(\omega t + \phi_0) .$$

In our polarimeter, we observe the time dependence of positrons in either the upstream or downstream hemispheres rather than along some specified direction. This is equivalent to integrating our density function over a hemisphere, which we will take to be $-\pi/2 < \phi < \pi/2$, $0 < x < 1$, $0 < \theta < \pi$. This gives

$$R(t) = \int_0^1 dx \int_0^{\pi} d\theta \int_{-\pi/2}^{\pi/2} d\phi \left(\frac{d^3N}{dx d^2\Omega} \right) .$$

We now assume that $\eta(\theta, \phi, x)$ only depends on x and θ_{dip} , the dip angle into the aluminum plate. Since $0 < \theta_{dip} < \frac{\pi}{2}$ and $\cos\theta_{dip} = \sin\theta\cos\phi$,

$$\eta = \eta(\cos\theta_{dip}, x) = \eta(\sin\theta\cos\phi, x) .$$

Since η is even in ϕ while $\sin\phi$ is odd in ϕ ,

$$\int_{-\pi/2}^{\pi/2} d\phi \sin\phi \eta = 0$$

so the term in $d^3N/dxd^2\Omega$ containing the factor $\sin(\omega t + \phi_0)$ has a vanishing integral.

Also, since $\eta(\theta) = \eta(\pi - \theta)$,

$$\int_0^{\pi} \eta(\theta) \cos\theta d\theta = 0$$

so the term in $d^3N/dxd^2\Omega$ containing the factor $\cos\theta$ has a vanishing integral. This leaves us with

$$R(t) = \int \eta f + \sin\theta_{\mu} \cos(\omega t + \phi_0) \int \eta g \sin\theta \cos\phi \quad .$$

If $R(t)$ is to have the form

$$R(t) = c \left[1 + \alpha \cos(\omega t + \phi_0) \right]$$

then

$$\alpha = \sin\theta_{\mu} \frac{\int \sin\theta \cos\phi \eta g}{\int f \eta} \quad .$$

If $\eta(\theta, \phi, x)$ has a fixed functional form, then the integrals in α will just be constants. This is not the case, since the form of η clearly depends on the depth into the aluminum plate that the muon has penetrated. If this depth is s , then

$$\alpha = \sin\theta_{\mu} F(s)$$

for some function F .

We do not know what s is for any particular event, but for a large enough collection of events, we can replace $F(s)$ by its average value.

APPENDIX B

Polarimeter Time Distribution Including Poisson Background

The polarimeter time distribution is complicated by the presence of Poisson-distributed background and by the requirements demanded by the logic for a positron signal. The latter condition means that the time distributions of upstream or downstream emitted positrons must be considered together since, for example, an upstream decay signal occurring after a downstream decay signal will be ignored.

In the following discussion, the time distributions will be understood to be probability distributions for detecting a positron signal at time t , given that a muon has stopped in the polarimeter. The muon stops at time $t = 0$ and the electronics gate opens at $t = t_0$. The subscripts b and f will label quantities related to the backward (upstream) or forward (downstream) positron signals. We shall calculate the time distributions for the backwards signals -- the forward distribution is obtained by reversing f and b everywhere.

Let

$$R_b(t) = n_b e^{-t/\tau} \left[1 + \alpha_b \cos(\omega t + \phi) \right]$$

be the distribution of real backward-emitted positrons, with a similar expression for forward decays. Also let λ_b and λ_f be the rate of spurious backward and forward positron signals. The resulting observed

time distribution for backward positron signals is then

$$S_b(t) = e^{-\lambda_b(t-t_0)} e^{-\lambda_f(t-t_0)} \left\{ R_b(t) + \lambda_b \left[1 - \int_{t_0}^t R_b(t) - \int_{t_0}^t R_f(t) \right] \right\} .$$

The exponentials are the probabilities that no spurious signals are detected before time t in either direction, forward or backward. At t , the observed signal could be real or false. If it is false, it cannot be preceded by an earlier real signal. This is provided for by the time integrals of R .

So, plugging and chugging,

$$S_b(t) = e^{-(\lambda_b + \lambda_f)(t-t_0)} \left\{ \eta_b e^{-t/\tau} \left[1 + \alpha_b \cos(\omega t + \phi) \right] + \lambda_b \left[1 - (\eta_b + \eta_f) \int_{t_0}^t e^{-t/\tau} dt - (\eta_b \alpha_b + \eta_f \alpha_f) \int_{t_0}^t e^{-t/\tau} \cos(\omega t + \phi) dt \right] \right\}$$

But

$$\int_{t_0}^t e^{-t/\tau} \cos(\omega t + \phi) dt = \frac{e^{-t/\tau} \left[\omega \sin(\omega t + \phi) - \frac{1}{\tau} \cos(\omega t + \phi) \right]}{(\omega^2 + 1/\tau^2)} - \frac{e^{-t_0/\tau} \left[\omega \sin(\omega t_0 + \phi) - \frac{1}{\tau} \cos(\omega t_0 + \phi) \right]}{(\omega^2 + 1/\tau^2)} .$$

So

$$S_b(t) = e^{-(\lambda_b + \lambda_f)t} \left\{ A + e^{-t/\tau} \left[B + C \cos(\omega t + \phi) + D \sin(\omega t + \phi) \right] \right\}$$

where

$$A = e^{(\lambda_b + \lambda_f)t_0} \lambda_b \left[1 - (\eta_b + \eta_f)\tau e^{-t_0/\tau} + \frac{(\eta_b \alpha_b + \eta_f \alpha_f)}{(\omega^2 + 1/\tau^2)} e^{-t_0/\tau} \left(\omega \sin(\omega t_0 + \phi) - \frac{1}{\tau} \cos(\omega t_0 + \phi) \right) \right]$$

$$B = e^{(\lambda_b + \lambda_f)t_0} \left[\eta_b + \lambda_b (\eta_b + \eta_f)\tau \right]$$

$$C = e^{(\lambda_b + \lambda_f)t_0} \left[\eta_b \alpha_b + \frac{\lambda_b (\eta_b \alpha_b + \eta_f \alpha_f)}{\tau (\omega^2 + 1/\tau^2)} \right]$$

and

$$D = -e^{(\lambda_b + \lambda_f)t_0} \lambda_b \omega (\eta_b \alpha_b + \eta_f \alpha_f) / (\omega^2 + 1/\tau^2)$$

In our analysis, we parameterize the data with the somewhat simpler form

$$S(t) = e^{-\lambda t} \left\{ N e^{-t/\tau} \left[1 + \alpha \cos(\omega t + \phi) \right] + \Lambda \right\}$$

which does not include a sine term. This introduces a small phase shift of γ to ϕ . Let E be defined by

$$E \cos(\omega t + \phi + \gamma) = C \cos(\omega t + \phi) + D \sin(\omega t + \phi)$$

Then $\gamma \cong \tan \gamma = -D/C$ or

$$\gamma \cong (\lambda_b \tau)(\omega \tau) / \left[\left(\frac{1 + \omega^2 \tau^2}{1 + \frac{\alpha_f \eta_f}{\alpha_b \eta_b}} \right) + \lambda_b \tau \right]$$

For this experiment, $\alpha_f \cong \alpha_b$, $\eta_f \cong \eta_b$, $\omega\tau = 18.8$ and $\lambda_b\tau \cong 0.006$. Then, using $\lambda_b\tau < 0.01$ to be conservative, $\gamma < 0.001$.

Besides being small, γ is always positive and so acts like an error in zero-time (see Section E of Chapter IV). Hence by periodically reversing the precessing field, its effect on the determination of ϕ will cancel out.

APPENDIX C

Estimated Phase Error Due to Polarimeter Inefficiency and Nonuniformity

The i th muon stopping in the polarimeter has a downstream (+) or upstream (-) time distribution

$$r_i^\pm(t) = N_i^\pm e^{-t/\tau} \left[1 \pm A_i^\pm \hat{s}_i(t) \cdot \hat{z} \right]$$

where N is the overall normalization, A is the asymmetry parameter, $\hat{s}(t)$ is the muon's polarization, \hat{z} is the axis in the precession plane which acts as the origin for the azimuthal angle, and τ is the muon's lifetime. The positron time distributions $R^\pm(t) = \sum_i r_i^\pm(t)$ accumulated over the data sample, will have an initial phase ϕ that is equal to the azimuthal angle of the vector

$$\vec{V} = \sum_i (N_i^+ A_i^+ + N_i^- A_i^-) \hat{s}_i(0) \quad .$$

In this experiment, we compute a vector, call it \vec{U} , which is the sum of \hat{s}_i for events with an observed muon decay. We wish to show how nearly parallel \vec{U} is to \vec{V} .

The probability that the i th muon's decay will be seen is

$$w_i = \int_{t_0}^{t_1} \left[r_i^+(t) + r_i^-(t) \right] dt$$

where the electronics gate is open from t_0 to t_1 . Then

$$\hat{U} = \sum_{i \in I} \hat{s}_i = \sum_i w_i \hat{s}_i$$

where I is the set of events with observed muon decays.

Integrating, with $\hat{s}_i(t) \cdot \hat{z} = \sin\theta_i \cos(\omega t + \phi_i)$,

$$w_i = -\tau e^{-t_1/\tau} (N_i^+ + N_i^-) \left\{ 1 - \left[\omega \tau \sin(\omega t_1 + \phi_i) - \cos(\omega t_1 + \phi_i) \right] \left(\frac{N_i^+ A_i^+ - N_i^- A_i^-}{N_i^+ + N_i^-} \right) \frac{\sin\theta_i}{(1 + \omega^2 \tau^2)} \right\} \\ + \tau e^{-t_0/\tau} (N_i^+ + N_i^-) \left\{ 1 - \left[\omega \tau \sin(\omega t_0 + \phi_i) - \cos(\omega t_0 + \phi_i) \right] \left(\frac{N_i^+ A_i^+ - N_i^- A_i^-}{N_i^+ + N_i^-} \right) \frac{\sin\theta_i}{(1 + \omega^2 \tau^2)} \right\}$$

The terms involving θ_i and ϕ_i are unpleasant, since they imply that the weighting factor w_i depends on \hat{s}_i . However, these terms are negligibly small as shown by the following analysis. Let

$$x \equiv \left(\frac{N_i^+ A_i^+ - N_i^- A_i^-}{N_i^+ + N_i^-} \right) \frac{\sin\theta_i}{(1 + \omega^2 \tau^2)} \left[\omega \tau \sin(\omega t_1 + \phi_i) - \cos(\omega t_1 + \phi_i) \right]$$

But $\omega \tau = 18.85$ and $|\sin\theta_i| < 1$ and $A_i^\pm \cong 0.32$, and

$$|\omega \tau \sin(\omega t_1 + \phi_i) - \cos(\omega t_1 + \phi_i)| < \sqrt{1 + \omega^2 \tau^2}$$

and

$$\frac{N_1^+ A_1^+ - N_1^- A_1^-}{N_1^+ + N_1^-} = \left(\frac{A_1^+ + A_1^-}{2} \right) \left[\left(\frac{N_1^+ - N_1^-}{N_1^+ + N_1^-} \right) + \left(\frac{A_1^+ - A_1^-}{A_1^+ + A_1^-} \right) \right]$$

So

$$|x| < 0.017 \left[\left(\frac{N_1^+ - N_1^-}{N_1^+ + N_1^-} \right) + \left(\frac{A_1^+ - A_1^-}{A_1^+ + A_1^-} \right) \right]$$

We now exploit the multilayered design of the polarimeter to claim that the two asymmetry terms above will tend to vanish when summed over a large sample of events. The stopping position of a muon in the z direction is more a function of the K_L^0 momentum than the $K_{\mu 3}$ configuration. The relatively high muon transverse momentum required by our acceptance restricts the range of the muon's C.O.M. energy and longitudinal momentum. Hence for every muon that stops in the m^{th} aluminum plate and decays downstream, we can imagine another muon with the same polarization and transverse coordinates that stopped in the $(m+2)^{\text{th}}$ plate and decayed upstream. For these two decays, N and A are identical.

More explicitly, suppose we change the event label to include which plate the muon stopped in. For example, $r_{mj}^{\pm}(t)$ is the time distribution for the j^{th} muon that stopped in the m^{th} plate. Then

$$w_{mj} = \int_{t_0}^{t_1} \left[r_{mj}^+(t) + r_{mj}^-(t) \right] dt$$

and

$$\vec{U} = \sum_m \sum_j \left[\int_{t_0}^{t_1} r_{mj}^+(t) dt + \int_{t_0}^{t_1} r_{mj}^-(t) dt \right] \hat{s}_{mj}$$

But now m is a dummy variable, so

$$\vec{U} = \sum_m \sum_j \left[\hat{s}_{m-1,j} \int_{t_0}^{t_1} r_{m-1,j}^+(t) dt + \hat{s}_{m+1,j} \int_{t_0}^{t_1} r_{m+1,j}^-(t) dt \right] .$$

The statement that the polarization distribution is approximately z -independent, especially over the short distance of two plates, means that we can order the events such that $\hat{s}_{m-1,j} \cong \hat{s}_{m+1,j}$:

$$\vec{U} \cong \sum_m \sum_j \hat{s}_{m\pm 1,j} \int_{t_0}^{t_1} \left[r_{m-1,j}^+(t) + r_{m+1,j}^-(t) \right] dt$$

which looks like our previous expression of \vec{U} except that now we can say

$$N_{m-1,j}^+ = N_{m+1,j}^-$$

$$A_{m-1,j}^+ = A_{m+1,j}^-$$

except near the front or rear of the polarimeter, and if the longitudinal distribution of the stopped muons is not uniform.

The polarimeter has thirty aluminum plates, but only muons stopping in plates 2 through 29 are counted. Therefore, N_{2j}^- , N_{3j}^- , N_{28j}^+ , and N_{29j}^+ are not exactly balanced. This represents 4/28 of the data. At worst, if

$$\frac{N_{28j}^+ - N_{3j}^-}{N_{28j}^+ + N_{3j}^-} = \frac{N_{29j}^+ - N_{2j}^-}{N_{29j}^+ + N_{2j}^-} = 1$$

(and ignoring any asymmetry in the A's, which is expected to be very small), then

$$|x| \gtrsim 0.017 \times (4/28) = 0.0024$$

which is already down to the level of 2 or 3 milliradians, which is sufficiently small to be negligible.

The same conclusion holds in the case of a non-uniform longitudinal plate distribution if the difference in the number of muons stopping in any two plates separated by one plate, divided by the sum, is less than 0.14. In fact, it is sufficient that the average of this quantity over all such plate pairs in the polarimeter be less than 0.14. The plate distribution of the stopped muons, shown in Figure 20, clearly shows that this condition is satisfied. In fact, the average is 0.018.

So, ignoring the angle-dependent terms,

$$w_i = \tau \left(e^{-t_0/\tau} - e^{-t_1/\tau} \right) (N_i^+ + N_i^-)$$

so that \vec{U} is parallel to $\sum_i (N_i^+ + N_i^-) \hat{s}_i \cong 2 \sum_i N_i \hat{s}_i$. But

$$\vec{V} = \sum_i (N_i^+ A_i^+ + N_i^- A_i^-) \hat{s}_i \cong 2 \sum_i N_i A_i \hat{s}_i$$

so \vec{U} is parallel to \vec{V} if A_i is constant over the polarimeter.

Alternatively, over the data sample, the expected values of \vec{U} and \vec{V} are

$$\langle \vec{U} \rangle \propto \left\langle \sum_i (N_i^+ + N_i^-) \hat{s}_i \right\rangle = \sum_i \langle (N_i^+ + N_i^-) \rangle \langle \hat{s}_i \rangle \propto \langle \hat{s}_i \rangle$$

if \hat{s}_i is uncorrelated with N_i^\pm , and

$$\langle \hat{\psi} \rangle = \sum_j \langle N_j^+ A_j^+ + N_j^- A_j^- \rangle \langle \hat{s}_j \rangle \propto \langle \hat{s}_j \rangle$$

if \hat{s}_j is uncorrelated with N_j^{\pm} and A_j^{\pm} .

Hence $\langle \hat{U} \rangle \propto \langle \hat{\psi} \rangle$.

APPENDIX D

Probabilities of the Two Possible Event Configurations

For each $K_{\mu 3}$ event, we measure nine quantities in the laboratory: \vec{P}_{π} and \vec{P}_{μ} , the momenta of the two charged secondaries, and \vec{r}_D , the position of the decay vertex relative to the production target. We will find it convenient to use the variables z_D and $\vec{\Omega}_K$ in place of \vec{r}_D , where $z_D = |\vec{r}_D|$ and $\vec{\Omega}_K$ is the kaon momentum direction.

This set of variables is not sufficient to reconstruct the event completely, leading instead to a two-fold ambiguity. One of the features of this ambiguity is the two distinct values that P_K can assume. Resolving the ambiguity is equivalent to determining P_K .

For notational purposes, starred quantities are measured in the K_L^0 rest frame, while unstarred quantities are either invariant or measured in the laboratory. \vec{P}_{KA} and \vec{P}_{KB} are the two kaon momenta consistent with L , where L is the configuration of the observed variables. $\text{Pr}(\vec{P}_K)$ is the probability of generating a kaon at the production target with momentum \vec{P}_K ; and $\text{Pr}(X|Y)$ is the conditional probability for X occurring, given that Y has occurred.

Now, applying the Golden Rule, we can get the probability for a decay to occur in a differential volume of phase space in the kaon rest frame:

$$\phi \propto |M|^2 \frac{d^3p_{\pi}^*}{E_{\pi}^*} \frac{d^3p_{\mu}^*}{E_{\mu}^*} \frac{d^3p_{\nu}^*}{E_{\nu}^*} e^{-t^*/\tau} dt^* \delta^4(q_K - q_{\pi} - q_{\mu} - q_{\nu})$$

where $|M|^2$ is the squared matrix element, τ is the muon lifetime, and the q 's are four-momenta.

If we now specify \vec{P}_K , we can transform the kaon frame decay distribution ϕ into the appropriate laboratory distribution $\text{Pr}(L|\vec{P}_K)$. Operationally, a function of kaon frame variables becomes transformed into a function of the corresponding laboratory variables. We first observe that: (1) d^3p/E is an invariant form so, for example,

$$\frac{d^3p_\pi^*}{E_\pi^*} = \frac{d^3p_\pi}{E_\pi}$$

and (2)

$$t^* = t/\gamma = z_D/\beta\gamma = M_K z_D/P_K$$

so that $dt^* = (M_K/P_K)dz_D$. (Recall that P_K is not a variable but a specified parameter.) Hence

$$\text{Pr}(L|\vec{P}_K) \propto |M|^2 \frac{d^3p_\pi}{E_\pi} \frac{d^3p_\mu}{E_\mu} \frac{d^3p_\nu}{E_\nu} e^{-\frac{M_K z_D}{P_K \tau}} \left(\frac{M_K}{P_K}\right) dz_D \delta^4(q_K - q_\pi - q_\mu - q_\nu).$$

The probability of producing a kaon with momentum \vec{P}_K is

$$\text{Pr}(\vec{P}_K) = N(P_K) dP_K d^2\Omega_K$$

where $N(P_K)$ is the beam momentum spectrum at the production target. The angular dependence of N is ignored, since the spectrum of P_K is sufficiently constant over the small solid angle subtended by our beam.

The probability of finding both an event in a particular laboratory configuration L and the kaon with momentum \vec{P}_K is

$$\begin{aligned} \text{Pr}(L \cdot \vec{P}_K) &= \text{Pr}(L | \vec{P}_K) \text{Pr}(\vec{P}_K) \\ &= |M|^2 N(P_K) e^{-\frac{M_K z_D}{P_K \tau} \left(\frac{1}{P_K}\right) \frac{d^3 P_\pi}{E_\pi} \frac{d^3 P_\mu}{E_\mu} \frac{d^3 P_\nu}{E_\nu} dz_D dP_K d^2 \Omega_K \delta^4(Q)}. \end{aligned}$$

We must integrate over the unobserved variables \vec{P}_ν and P_K to eliminate the delta function constraint. Using the three-momentum part of the delta function, the integral over $d^3 P_\nu$ is eliminated straightaway. The remaining delta function can be used to eliminate the integral over P_K through the relation

$$\int F(P_K) \delta(g(P_K)) dP_K = \frac{F(P_K)}{\left| \frac{\partial g}{\partial P_K} \right|} \Bigg|_{g(P_K) = 0}$$

with $g(P_K) = E_K - E_\pi - E_\mu - E_\nu$. Then

$$\frac{\partial g}{\partial P_K} = \frac{\partial E_K}{\partial P_K} - \frac{\partial E_\nu}{\partial P_K} = \frac{P_K}{E_K} - \frac{\partial E_\nu}{\partial P_K}.$$

To evaluate $\partial E_\nu / \partial P_K$, we cannot yet assume energy conservation.

From three-momentum conservation, $\vec{P}_\nu = \vec{P}_K - \vec{P}_\pi - \vec{P}_\mu$. Then

$$P_\nu^2 = E_\nu^2 = P_K^2 + P_\pi^2 + P_\mu^2 - 2(\vec{P}_K \cdot \vec{P}_\pi + \vec{P}_K \cdot \vec{P}_\mu - \vec{P}_\pi \cdot \vec{P}_\mu).$$

Therefore

$$\frac{\partial E_\nu}{\partial P_K} = \left[P_K - \frac{\vec{P}_K \cdot (\vec{P}_\pi + \vec{P}_\mu)}{P_K} \right] / E_\nu$$

and

$$\frac{\partial g}{\partial P_K} = \left[-\frac{P_K(E_\pi + E_\mu)}{E_K} + \frac{\vec{P}_K \cdot (\vec{P}_\pi + \vec{P}_\mu)}{P_K} \right] / E_\nu$$

where we used $E_\nu = E_K - E_\pi - E_\mu$ as now specified by $g(P_K) = 0$.

Hence

$$\Pr(L \cdot \vec{P}_K) = \frac{|M|^2 N(P_K) e^{-\frac{M_K z_D}{P_K T}} d^3 p_\pi d^3 p_\mu d^2 \Omega_K dz_D}{E_\pi E_\mu |\vec{P}_K \cdot (\vec{P}_\pi + \vec{P}_\mu) - P_K^2 (E_\pi + E_\mu) / E_K}$$

If we are given a laboratory configuration L , there are two and only two mutually exclusive possible values for the kaon momentum -- \vec{P}_{KA} and \vec{P}_{KB} . Applying Bayes' Theorem,²⁰ the probability that the kaon momentum is \vec{P}_{KA} , given L , is

$$\begin{aligned} \Pr(\vec{P}_{KA} | L) &= \frac{\Pr(L | \vec{P}_{KA}) \Pr(\vec{P}_{KA})}{\Pr(L | \vec{P}_{KA}) \Pr(\vec{P}_{KA}) + \Pr(L | \vec{P}_{KB}) \Pr(\vec{P}_{KB})} \\ &= \frac{\Pr(L \cdot \vec{P}_{KA})}{\Pr(L \cdot \vec{P}_{KA}) + \Pr(L \cdot \vec{P}_{KB})} \end{aligned}$$

with a similar expression for $\Pr(\vec{P}_{KB} | L)$. Note that

$$\Pr(\vec{P}_{KA} | L) + \Pr(\vec{P}_{KB} | L) = 1 .$$

Finally, we observe that the proportionality constant in the expression for $\text{Pr}\{\vec{L} \cdot \vec{P}_K\}$ is irrelevant. Also, while the differential volume $d^3P_\pi d^3P_\mu d^2\Omega_K dz_D$ is of arbitrary size, it is equal for the two solutions, and so it can be absorbed into the proportionality constant.

APPENDIX E

Statistical Uncertainty of the Predicted Phase

For the i th event in a sample, let \hat{e}_{Ai} and \hat{e}_{Bi} be the two possible unit polarization vectors resulting from the quadratic ambiguity, with corresponding probabilities P_{Ai} and P_{Bi} . Also, denote \vec{e}_i as the random variable for the polarization vector. (So, for example, the probability is P_{Ai} that $\vec{e}_i = \hat{e}_{Ai}$.)

The resultant polarization vector for the entire sample is given by $\vec{r} = \sum_i \vec{e}_i$. If we let $\langle x \rangle$ denote the expected value of any x , then

$$\langle \vec{r} \rangle = \sum_i \langle \vec{e}_i \rangle = \sum_i (P_{Ai} \hat{e}_{Ai} + P_{Bi} \hat{e}_{Bi}) .$$

Now define $\Delta \vec{r} \equiv \vec{r} - \langle \vec{r} \rangle$ and $\Delta \vec{e}_i \equiv \vec{e}_i - \langle \vec{e}_i \rangle$. Then

$$\Delta \vec{r} = \sum_i \Delta \vec{e}_i \quad \text{and} \quad \langle |\Delta \vec{r}|^2 \rangle = \langle |\sum_i \Delta \vec{e}_i|^2 \rangle .$$

At this point, we digress to prove that $\langle \Delta \vec{e}_i \cdot \Delta \vec{e}_j \rangle = 0$ for $i \neq j$. To begin with, we note that

$$\Delta \vec{e}_i = \begin{cases} \hat{e}_{Ai} - (P_{Ai} \hat{e}_{Ai} + P_{Bi} \hat{e}_{Bi}) & \text{with probability } P_{Ai} \\ \hat{e}_{Bi} - (P_{Ai} \hat{e}_{Ai} + P_{Bi} \hat{e}_{Bi}) & \text{with probability } P_{Bi} \end{cases}$$

so, since $P_{Ai} + P_{Bi} = 1$,

$$\Delta \vec{e}_i = \begin{cases} P_{Bi}(\hat{e}_{Ai} - \hat{e}_{Bi}) & \text{with probability } P_{Ai} \\ P_{Ai}(\hat{e}_{Bi} - \hat{e}_{Ai}) & \text{with probability } P_{Bi} \end{cases}$$

Therefore, if i and j are two separate events,

$$\begin{aligned} \langle \Delta \vec{e}_i \cdot \Delta \vec{e}_j \rangle &= P_{Ai} P_{Aj} [P_{Bi}(\hat{e}_{Ai} - \hat{e}_{Bi}) \cdot P_{Bj}(\hat{e}_{Aj} - \hat{e}_{Bj})] \\ &+ P_{Ai} P_{Bj} [P_{Bi}(\hat{e}_{Ai} - \hat{e}_{Bi}) \cdot P_{Aj}(\hat{e}_{Bj} - \hat{e}_{Aj})] \\ &+ P_{Bi} P_{Aj} [P_{Ai}(\hat{e}_{Bi} - \hat{e}_{Ai}) \cdot P_{Bj}(\hat{e}_{Aj} - \hat{e}_{Bj})] \\ &+ P_{Bi} P_{Bj} [P_{Ai}(\hat{e}_{Bi} - \hat{e}_{Ai}) \cdot P_{Aj}(\hat{e}_{Bj} - \hat{e}_{Aj})] \\ &= 0 \end{aligned} \quad \text{Q.E.D.}$$

With this result, we immediately have that

$$\langle |\Sigma \Delta \vec{e}_i|^2 \rangle = \Sigma \langle |\Delta \vec{e}_i|^2 \rangle$$

Now

$$\begin{aligned} \langle |\Delta \vec{e}_i|^2 \rangle &= P_{Ai} (P_{Bi}^2 |\hat{e}_{Ai} - \hat{e}_{Bi}|^2) \\ &+ P_{Bi} (P_{Ai}^2 |\hat{e}_{Bi} - \hat{e}_{Ai}|^2) \\ &= P_{Ai} P_{Bi} |\hat{e}_{Ai} - \hat{e}_{Bi}|^2 \end{aligned}$$

Hence

$$\langle |\Delta \vec{r}|^2 \rangle = \sum_i P_{Ai} P_{Bi} |\hat{e}_{Ai} - \hat{e}_{Bi}|^2 .$$

Let us define $\sigma_r^2 \equiv \langle |\Delta \vec{r}|^2 \rangle$.

We can repeat the procedure for the components of r . For example, with the x component, $r_x = \vec{r} \cdot \hat{x} = \sum_i \vec{e}_i \cdot \hat{x}$. So $\langle r_x \rangle = \sum_i \langle \vec{e}_i \rangle \cdot \hat{x}$ and $\Delta r_x = r_x - \langle r_x \rangle = \sum_i \Delta \vec{e}_i \cdot \hat{x}$. And finally

$$\begin{aligned} \langle (\Delta r_x)^2 \rangle &= \sum_i \left\{ P_{Ai} \left[P_{Bi} (\hat{e}_{Ai} - \hat{e}_{Bi}) \cdot \hat{x} \right]^2 \right. \\ &\quad \left. + P_{Bi} \left[P_{Ai} (\hat{e}_{Bi} - \hat{e}_{Ai}) \cdot \hat{x} \right]^2 \right\} \\ &= \sum_i P_{Ai} P_{Bi} \left[(\hat{e}_{Ai} - \hat{e}_{Bi}) \cdot \hat{x} \right]^2 . \end{aligned}$$

Let us define $\sigma_x^2 \equiv \langle (\Delta r_x)^2 \rangle$. We note that $\sigma_r^2 = \sigma_x^2 + \sigma_y^2 + \sigma_z^2$.

Similarly, we can show that

$$\langle \Delta r_x \Delta r_z \rangle = \sum_i P_{Ai} P_{Bi} \left[(\hat{e}_{Ai} - \hat{e}_{Bi}) \cdot \hat{x} \right] \left[(\hat{e}_{Ai} - \hat{e}_{Bi}) \cdot \hat{z} \right] .$$

Now for precession about the y axis, the phase ϕ of the polarization vector is defined by $\tan \phi = r_x / r_z$. Differentiation gives

$$\sec^2 \phi d\phi = (r_z dr_x - r_x dr_z) / r_z^2 .$$

But $\sec^2 \phi = 1 + \tan^2 \phi = 1 + r_x^2 / r_z^2$, so

$$d\phi = (r_2 dr_x - r_x dr_2) / (r_x^2 + r_2^2)$$

$$\sigma_{\phi}^2 = \frac{r_2^2 \sigma_x^2 + r_x^2 \sigma_2^2 - 2r_x r_2 \langle \Delta r_x \Delta r_2 \rangle}{(r_x^2 + r_2^2)^2}$$

APPENDIX F

Characteristics of the Polarization Vector

In a rectangular xyz coordinate system, suppose the axis of spin quantization lies along the z direction. Let the amplitude be A for the spin to be polarized in the +z direction; and B for the -z direction. The resulting spinor is

$$\psi = A \begin{pmatrix} 1 \\ 0 \end{pmatrix} + B \begin{pmatrix} 0 \\ 1 \end{pmatrix} = \begin{pmatrix} A \\ B \end{pmatrix} \quad (\text{A.1})$$

with

$$A^* A + B^* B = 1 \quad . \quad (\text{A.2})$$

Note that $\psi^\dagger \psi = 1$.

Now suppose we wish to quantize the spin along some other arbitrary axis indicated by the unit vector \hat{n} . The projection operator for a spin polarization pointing in the direction \hat{n} is:²¹

$$P(\hat{n}) = \frac{1}{2} (1 + \vec{\sigma} \cdot \hat{n})$$

where the components of $\vec{\sigma}$ are the usual Pauli matrices:

$$\sigma_x = \begin{pmatrix} 0 & 1 \\ 1 & 0 \end{pmatrix} , \quad \sigma_y = \begin{pmatrix} 0 & -i \\ i & 0 \end{pmatrix} , \quad \sigma_z = \begin{pmatrix} 1 & 0 \\ 0 & -1 \end{pmatrix} .$$

At the same time, the projection operator for a state with the same spin polarization as ψ is the density matrix $\psi\psi^\dagger$. By solving the equation

$$\frac{1}{2} (1 + \vec{\sigma} \cdot \hat{n}) = \psi\psi^\dagger \quad (\text{A.3})$$

for \hat{n} , we can determine the direction of polarization of ψ . From equation (A.1),

$$\psi\psi^\dagger = \begin{pmatrix} A^*A & AB^* \\ A^*B & B^*B \end{pmatrix} .$$

Hence

$$\vec{\sigma} \cdot \hat{n} = \begin{pmatrix} n_z & n_x - in_y \\ n_x + in_y & -n_z \end{pmatrix} = \begin{pmatrix} 2A^*A - 1 & 2AB^* \\ 2A^*B & 2B^*B - 1 \end{pmatrix}$$

which gives

$$n_z = 2A^*A - 1$$

$$n_x = 2\text{Re}(A^*B)$$

$$n_y = 2\text{Im}(A^*B) .$$

With the use of equation (A.2), it is trivial to confirm that

$$n_x^2 + n_y^2 + n_z^2 = 1 .$$

The polar coordinates of \hat{n} can be derived from the Cartesian coordinates by the relations

$$n_z = \cos\theta$$

$$n_x = \sin\theta \cos\phi$$

$$n_y = \sin\theta \sin\phi \quad .$$

Then, using equation (A.2),

$$\cos\theta = 2A^*A - 1 = (R^2 - 1)/(R^2 + 1)$$

where

$$R = |A|/|B| \quad .$$

Hence the polar angle θ is a function only of $|A|/|B|$. Also

$$\tan\phi = \frac{n_y}{n_x} = \frac{\text{Im}(A^*B)}{\text{Re}(A^*B)} \quad .$$

We recall that the overall phase of ψ has no physical significance, so we can choose A to be real and re-express $B = |B|e^{i\alpha}$ in terms of the relative phase α . Then

$$\tan\phi = \tan\alpha \quad .$$

Hence the azimuthal angle of the spin polarization is determined by the relative phase between A and B .

Since the spin state is described by a single spinor ψ , the spin is completely polarized. We can see this explicitly if we project ψ onto the direction of $-\hat{n}$. From equation (A.3) we get

$$P(-\hat{n}) = \frac{1}{2} (1 - \vec{\sigma} \cdot \hat{n}) = 1 - \psi\psi^\dagger$$

so

$$P(-\hat{n})\psi = (1 - \psi\psi^\dagger)\psi = 0 \quad .$$

The polarization along \hat{n} is then

$$s(\hat{n}) = \frac{|P(\hat{n})\psi|^2 - |P(-\hat{n})\psi|^2}{|P(\hat{n})\psi|^2 + |P(-\hat{n})\psi|^2} = 1 \quad .$$

We can also rewrite this as

$$s(\hat{n}) = (\bar{\psi} \vec{\sigma} \psi) \cdot \hat{n} = 1 \quad .$$

REFERENCES

1. G. Donaldson, D. Fryberger, D. Hitlin, J. Liu, B. Meyer, R. Piccioni, A. Rothenberg, D. Uggla, S. Wojcicki, and D. Dorfan, *Phys. Rev. Lett.* 31, 337 (1973).
2. M.K. Gaillard and L.M. Chouet, CERN 70-14 (1970).
3. N. Cabibbo and A. Maksymowicz, *Phys. Lett.* 9, 352 (1964); 11, 360 (1964); 14, 72 (1965).
4. P.B. Jones, *Progress in Nuclear Physics* 12, 8 (1969).
5. A.O. Weissenberg, *Muons* (North Holland Pub. Co., Amsterdam, 1967), page 47.
6. Particle Data Group, *Review of Particle Properties*, LBL-100, 4 (1974).
7. H.J. Frisch, *Stringent Limits on the Decays $K_L^0 \rightarrow \mu^+ \mu^-$, $e^+ e^-$, $\mu^\pm e^\mp$* , (Ph.D. Thesis), UCRL-20264, March 1971.
8. D.E. Coyle, R.C. Field, J.T. Gunn, and J.T. Tanabe, *Nucl. Inst. and Meth.* 95, 557 (1971).
9. R.C. Field, Bev-1039 (Internal document of the Accelerator Division, LBL).
10. R. Johnson and G. Shen, Addendum to Bev-3030 (Internal document of the Accelerator Division, LBL).
11. Chemical Rubber Corporation, *Handbook of Chemistry and Physics*, 46th Edition, page E-95.

12. Proc. of the Meeting on Muons in Solid State Physics, Burgenstock, 87 (1971).
13. D.G. Andrianov, G.G. Myasishcheva, Yu. V. Obukhov, V.S. Roganov, V.G. Firsov, and V.I. Fistul, Soviet Physics JETP 29, 643 (1969).
14. I.V. Iakovleva, Soviet Physics JETP 8, 676 (1959).
15. V.G. Nosov and I.V. Yakovleva, Soviet Physics JETP 16, 1236 (1963).
16. Lawrence Radiation Laboratory Counting Handbook, UCRL-3307, revised edition (unpublished).
17. A. Buhler, T. Massam, Th. Muller, M. Schneegans, and A. Zichichi, Il Nuovo Cimento 39, 824 (1965).
18. E.S. Ginsberg and J. Smith, Phys. Rev. D8, 3887 (1973).
19. C.Y. Chien, B. Cox, L. Ettlinger, L. Resvanis, R.A. Zdanis, E. Dally, P. Innocenti, E. Seppi, C.D. Buchanan, D.J. Drickey, F.D. Rudnick, P.F. Shepard, D.H. Stork, and H.K. Ticho, Phys. Lett 33B, 627 (1970).
20. R.S. Burington and D.C. May, Jr., Handbook of Probability and Statistics with tables, 2nd Ed., page 51 (1970).
21. T.D. Lee and C.S. Wu, Annual Rev. of Nucl. Sci. 16, 479 (1966).

TABLE 1. Previous Measurements of $\xi(0)^a$.

Author Code and Year	$\xi(0)$	Error	Type of Kaon
<u><i>Dalitz Plot Studies</i></u>			
Merlan 74	-0.57	0.24	charged
ABBC1 73	-0.36	0.40	"
Donaldson 73	0.01	0.04	neutral
Albrow 72	-1.5	0.7	"
Chiang 72	0.45	0.28	charged
Ankenbrandt 72	-0.62	0.28	"
Haidt 71	-1.1	0.56	"
Kijewski 69	-0.5	0.8	"
Callahan 66	0.72	0.93	"
<u><i>Branching Ratio</i></u>			
Evans 73	-0.08	0.25	neutral
Brandenburg 73	0.5	0.4	"
Chiang 72	0.0	0.15	charged
Haidt 71	-0.81	0.27	"
Botterill 70	-0.35	0.22	"
Basile 70	-0.5	0.5	neutral
Beilliere 69	0.45	0.28	"
Zeller 69	0.91	0.82	charged
Garland 68	1.0	0.6	"
<u><i>Polarization</i></u>			
Sandweiss 73	-0.385	0.105	neutral
Cutts 69	-0.95	0.3	charged
Longo 69	-1.81	0.5	neutral
Bettels 68	-1.0	0.3	charged

^aReference 6, pages 50, 56, and 57.

TABLE 2. Parameterized Fit To Data with All q^2 Bands Combined.

Parameter	Units	Pol. Field Up	Pol. Field Down
N^-		1909 ± 57	2079 ± 92
N^+		1454 ± 37	1619 ± 42
α^-		0.264 ± 0.015	0.293 ± 0.022
α^+		0.315 ± 0.016	0.322 ± 0.018
ϕ	radians	-0.719 ± 0.033	0.705 ± 0.029
ω	$10^6/\text{sec}$	8.304 ± 0.015	8.387 ± 0.014
τ	10^{-6}sec	2.26 ± 0.14	2.31 ± 0.12
Λ^-		193 ± 60	323 ± 93
Λ^+		132 ± 39	175 ± 47
λ^-	10^3	71 ± 40	107 ± 38
λ^+	10^3	42 ± 38	54 ± 33
χ^2/DOF		$124.9/137$	$191.0/137^a$
$\rho_{\phi\omega}$		-0.787	-0.776

^aThe purpose of this first fit (with all q^2 bands lumped together) is only to determine ω . The poor χ^2 here is caused by a few pathological bins at very early times, which apparently do not affect the frequency determination. By starting the fit from a later time bin, we got a χ^2 of 107.5 for 109 degrees of freedom, and a frequency of $\omega = 8.382 \pm 0.023$ megahertz.

TABLE 3. Phase Angle from Parameterized Fit
To Individual q^2 Bands (ω Fixed)

Polarimeter Field	q^2/m_x^2	χ^2 ^a	Polarization Phase ^b
down	4.45	129.0	0.9283 +0.0868 -0.0666
down	3.45	186.0	0.7807 +0.0456 -0.0453
down	2.45	148.1	0.6923 +0.0349 -0.0348
down	1.44	150.9	0.6688 +0.0282 -0.0281
down	0.84 ^c	127.5	0.5244 +0.0674 -0.0672
up	4.45	141.3	-0.9944 +0.0910 -0.0918
up	3.45	143.8	-0.8583 +0.0508 -0.0510
up	2.45	145.6	-0.7389 +0.0377 -0.0378
up	1.44	143.9	-0.6291 +0.0300 -0.0301
up	0.84 ^c	155.5	-0.6029 +0.0638 -0.0638

^a138 degrees of freedom.

^bPhases not corrected for possible zero-time error. See page 44.

^cNot used in final analysis (Table 4) because of large phase error and virtually no sensitivity to ξ .

TABLE 4. Determination of $\xi(q^2)$.

q^2/m_π^2	Polarization Phase	$\xi(q^2)$
1.439	0.6489 +0.0269 -0.0268	0.455 +0.941 -0.913
2.452	0.7156 +0.0310 -0.0309	0.204 +0.294 -0.301
3.448	0.8195 +0.0385 -0.0382	0.265 +0.171 -0.180
4.445	0.9614 +0.0660 -0.0654	0.104 +0.141 -0.154

TABLE 5. Sensitivity of $\xi(q^2)$ To Potential Systematic Errors.

q^2/m_π^2	Bin of q^2				
	1.44	2.45	3.45	4.45	All
Statistical error of $\xi(q^2)$	0.92	0.30	0.18	0.14	0.105
p_π raised 1%	-0.012	+0.007	-0.002	-0.014	-0.005
p_π lowered 1%	-0.035	-0.003	-0.002	+0.006	+0.001
p_μ raised 1%	+0.084	+0.016	+0.019	-0.015	+0.006
p_μ lowered 1%	-0.135	-0.029	-0.004	+0.003	-0.008
λ_+ set at 0.01	-0.018	+0.001	+0.020	+0.007	+0.011
λ_+ set at 0.02	-0.010	+0.001	+0.010	+0.003	+0.005
+5%/GeV ramp in P_K	+0.067	+0.043	+0.040	+0.031	+0.038
-5%/GeV ramp in P_K	-0.082	-0.044	-0.047	-0.035	-0.042

TABLE 6. Upper Limit Corrections for Contamination
of the $K_{\mu 3}$ Sample.

q^2/m_{π}^2	$\xi(q^2)$	$\Delta\xi$ for 90% efficient range device	$\Delta\xi$ for 95% efficient Cherenkov counter
1.44	0.45 ± 0.92	-0.031	-0.021
2.45	0.20 ± 0.30	-0.008	-0.012
3.45	0.26 ± 0.18	-0.002	-0.009
4.45	0.10 ± 0.14	-0.011	-0.010
All	0.178 ± 0.105	-0.007	-0.010

FIGURE CAPTIONS

- Figure 1. $K_{\mu 3}$ Dalitz plot with contours of the population density (relative scale) over the region visible to our apparatus.
- Figure 2. The direction of the muon polarization vector as a function of the position in the Dalitz plot for $\xi = 0$ (solid arrow) and $\xi = -1$ (dashed arrow). The sensitivity of the polarization to ξ is proportional to the opening angle between the two vectors. The muon momentum vector points to the right and the pion momentum lies in the lower half plane.
- Figure 3. Contours, indicating the acceptance of our apparatus (relative scale) as a function of position in the Dalitz plot.
- Figure 4. Plan view of the apparatus. T is the Chronotron, F and R are the upstream and downstream vertical hodoscopes, and H is the horizontal hodoscope.
- Figure 5. Elevation view of the neutral beamline.
- Figure 6. The picture frame magnets used to determine the momenta of secondaries in the two spectrometer arms.
- Figure 7. Exploded view of a spark chamber assembly.
- Figure 8. The range device and Cherenkov counter in the pion spectrometer.
- Figure 9. Momentum versus range in the range device.
- Figure 10. Schematic view of a section of the polarimeter.

Figure 11. Momentum versus range in the polarimeter.

Figure 12. Delayed signal interpretation in the polarimeter. The vertical lines represent scintillation counters. If one imagines time flowing downwards, then the x's indicate which counters produced a signal at various times. The muon enters from the left.

Figure 13. Flow diagram of our analysis procedure. The asterisks indicate paths taken at the conclusion of the data accumulation.

Figure 14. Monte Carlo result indicating the statistical phase error expected from a parameterized fit as a function of the time resolution.

Figure 15. Frequency versus time for decays in the polarimeter. The top half is a linear scale for comparing the goodness of fit at early times, while the lower half is a logarithmic scale for comparison at later times. (a) Polarimeter field pointing down; positron emitted in the upstream hemisphere. (b) Field down; downstream decay. (c) Field up; upstream decay. (d) Field up; downstream decay.

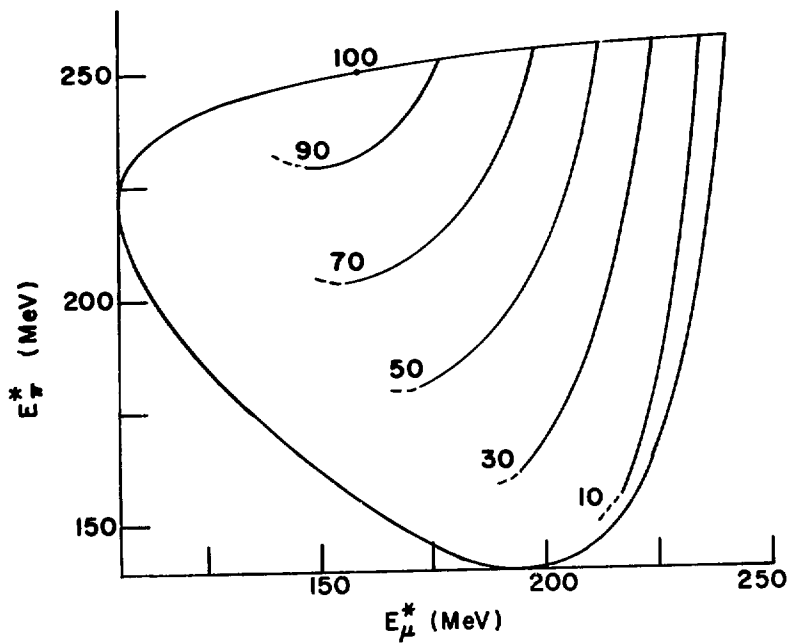
Figure 16. Predicted polarization phase as a function of ξ for the various bands of q^2 .

Figure 17. $\xi(q^2)$.

Figure 18. Comparison of our data expressed as $f_0(q^2)/f_+(0)$ with results of Donaldson, et al. (reference 1).

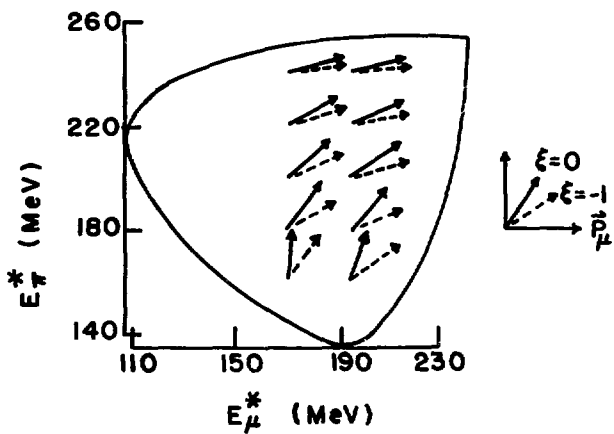
Figure 19. Event frequency versus $(p_0')^2$. Inset shows similar distribution from Chien, et al. (reference 19) for purposes of comparison only.

Figure 20. Event frequency (for events with the polarimeter field pointing down) as a function of polarimeter range. The vertical distance marked off in the center indicates the variation required between two different ranges for the difference divided by the sum of the events to equal 0.14. The depletion at the ends is due to momentum cuts.



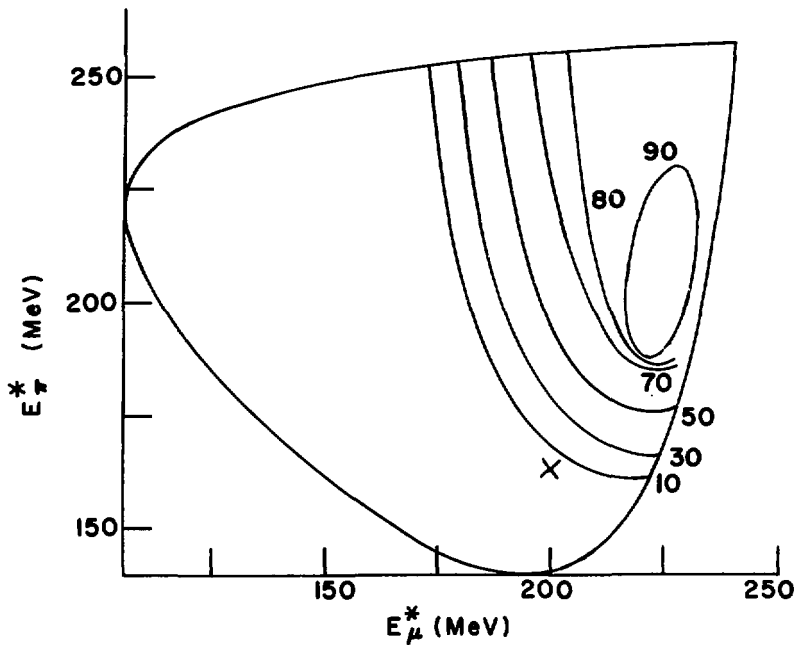
XBL 759-8188

Fig. 1



XBL 759-8190

Fig. 2



XBL 759-8187

Fig. 3

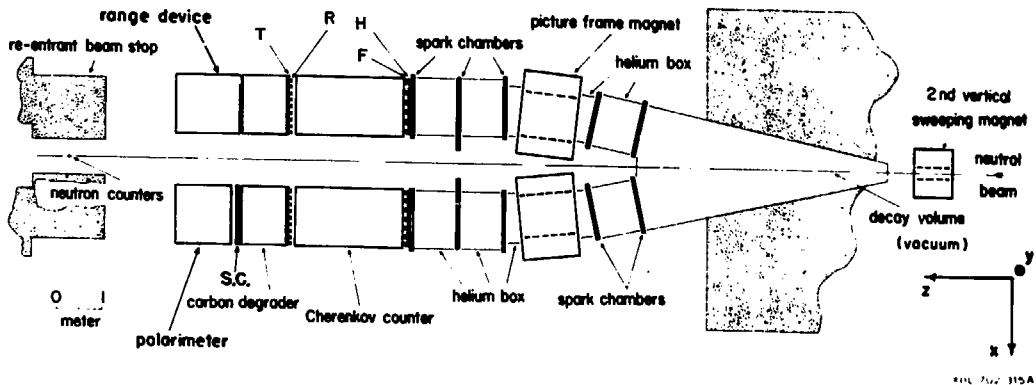
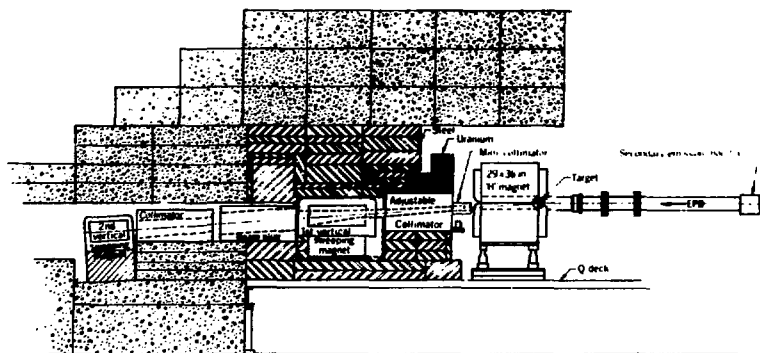
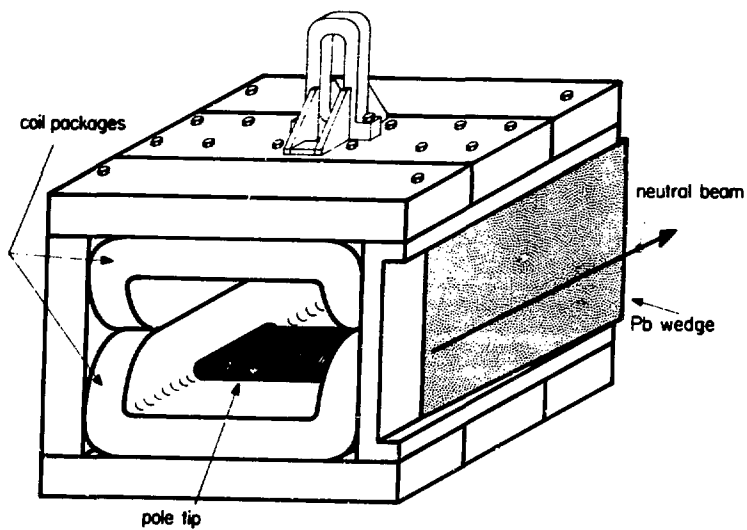


Fig. 4



KBL 703 0152

Fig. 5



XBL 702-440

Fig. 6

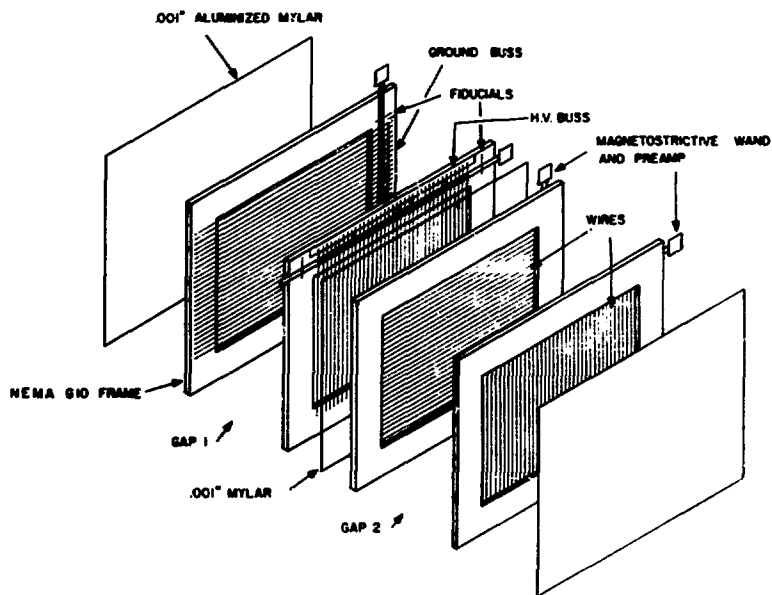


Fig. 7

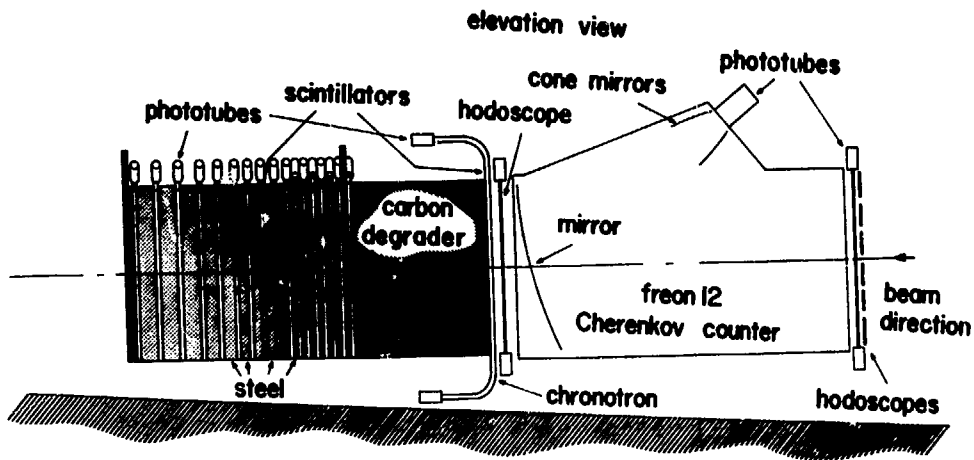
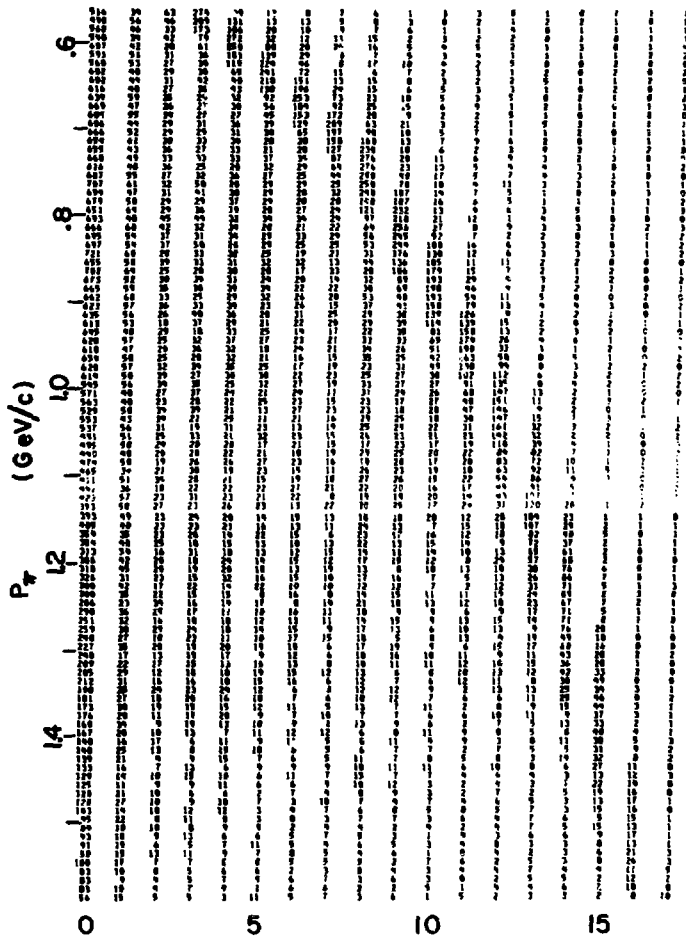


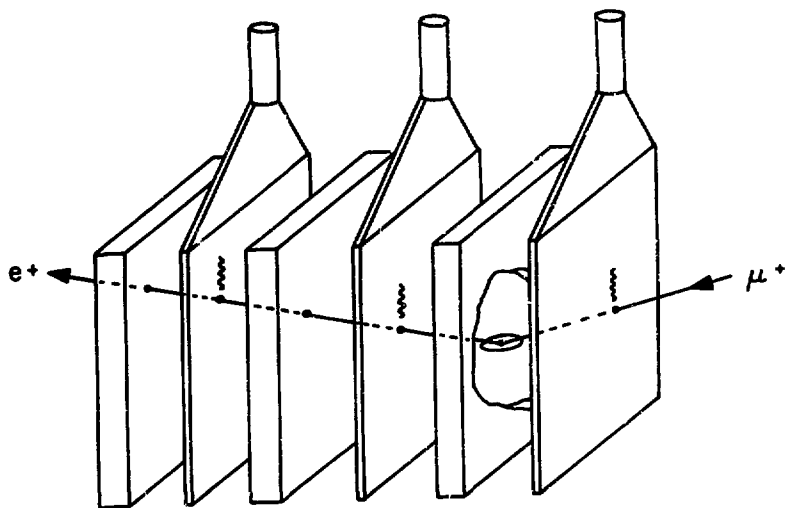
Fig. 8

XBL 702-316b



RANGE IN RANGE DEVICE (COUNTERS)

Fig. 9



XBL 759-8189

Fig. 10

P_{μ} (GeV/c)

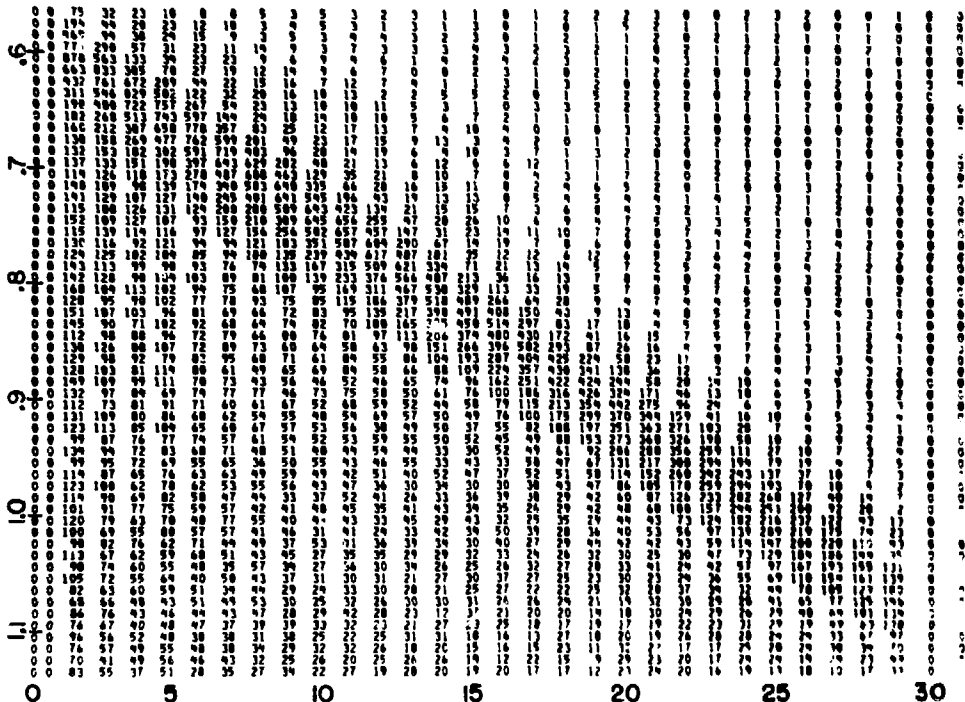
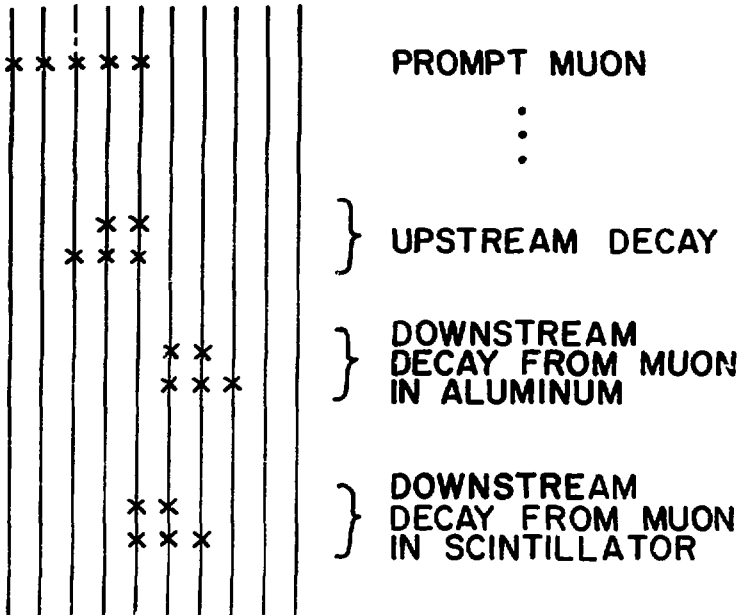


Fig. 11



NBL 759-8194

Fig. 12

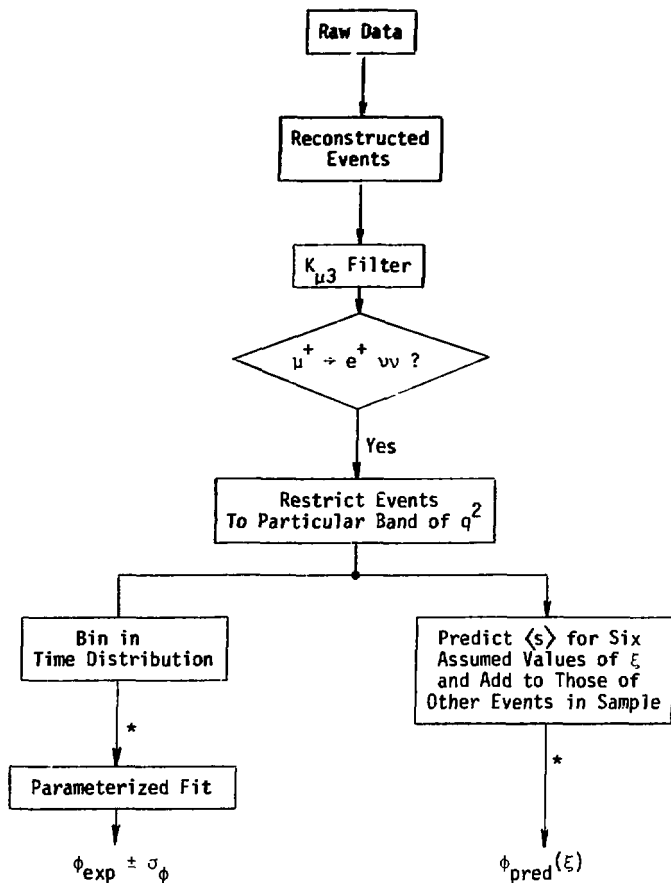
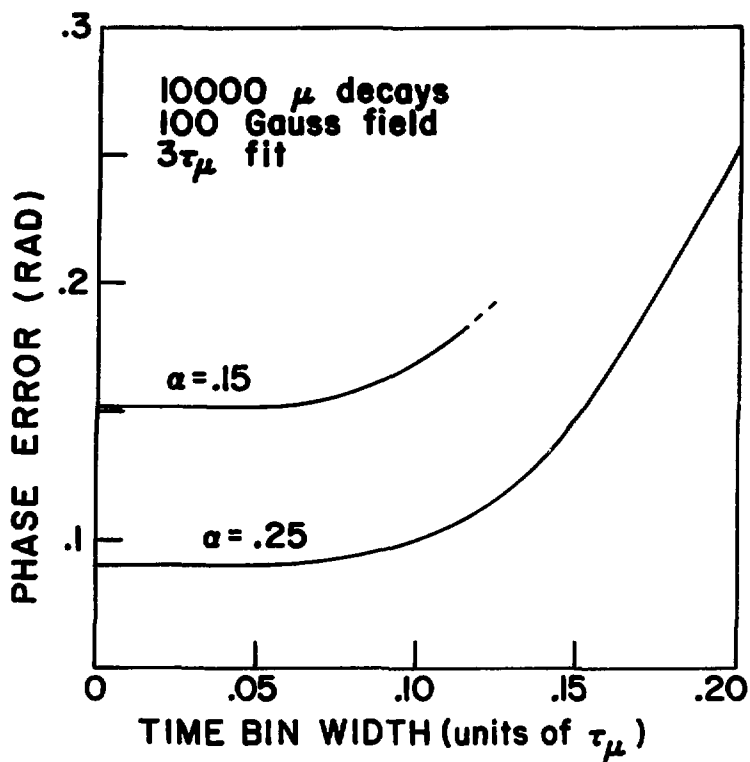


Fig. 13



XBL 759-8186

Fig. 14

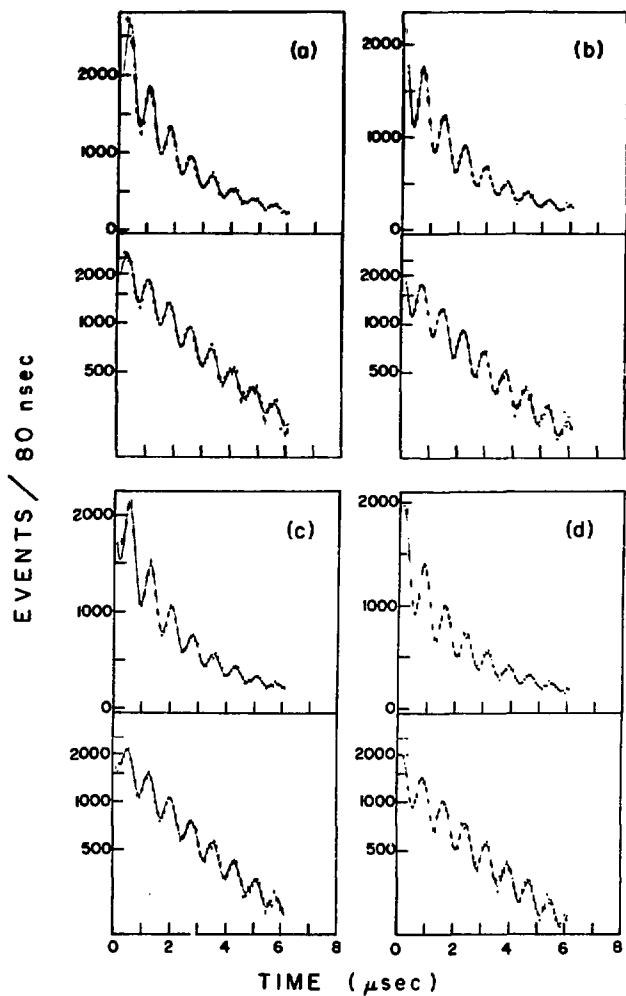


Fig. 15

NBL 759-8195

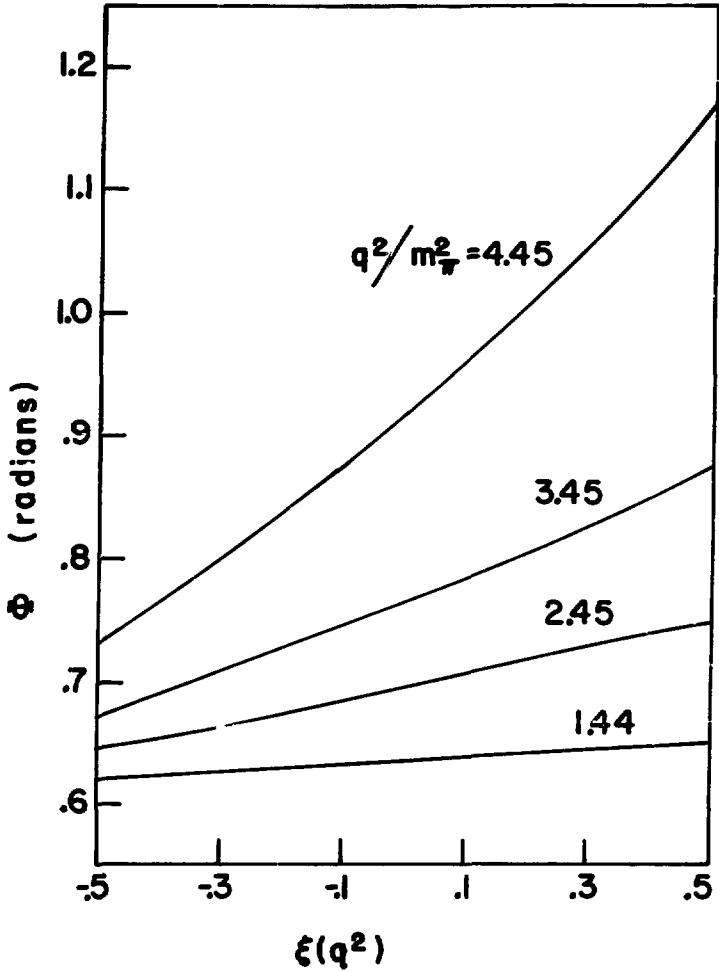
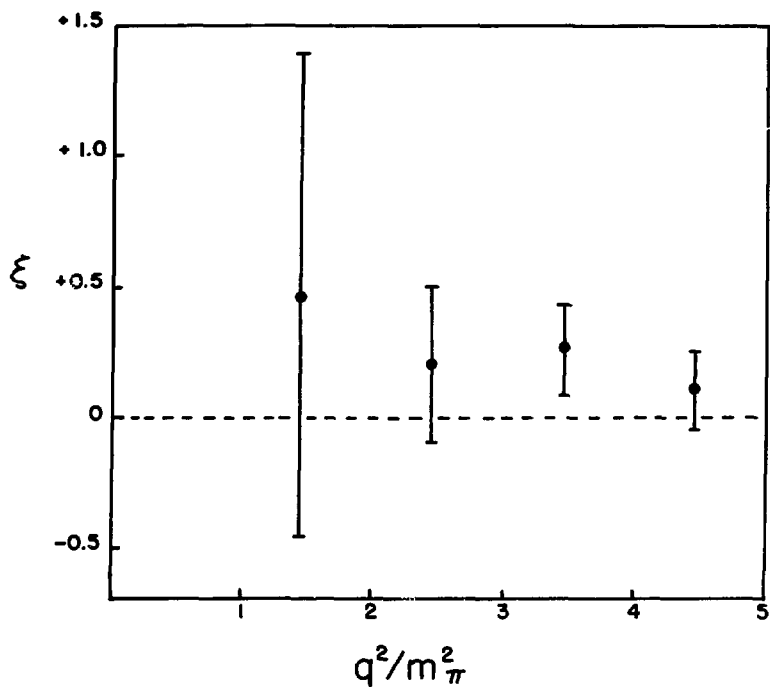


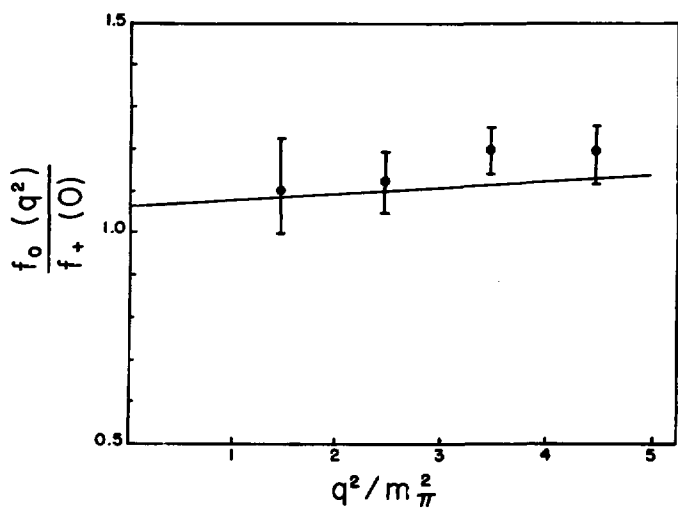
Fig. 16

XBL 759-8185



XBL 759-8184

Fig. 17



XBL 759-8182

Fig. 18

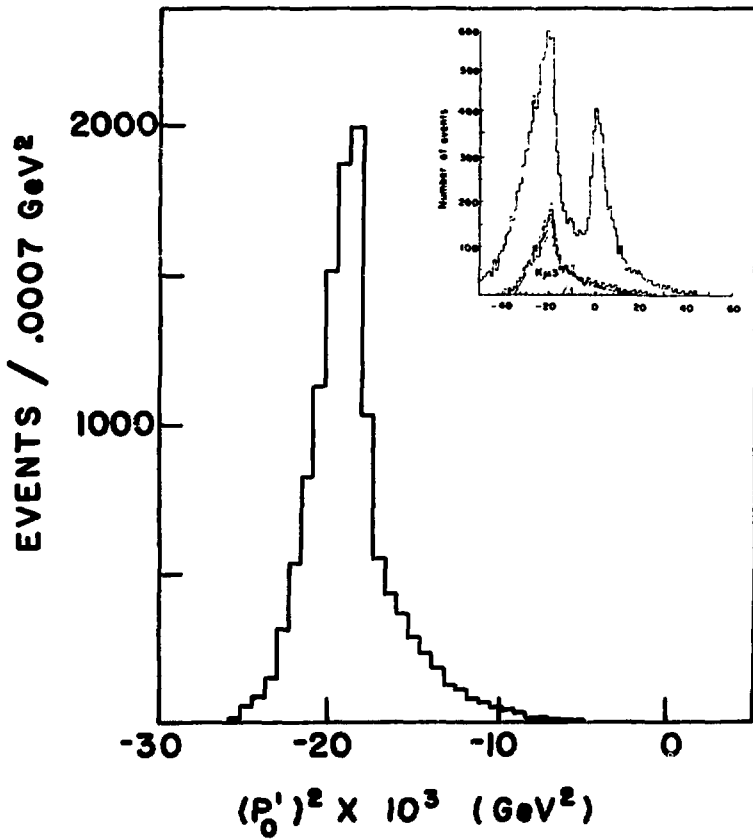


Fig. 19

XBL 759-8181

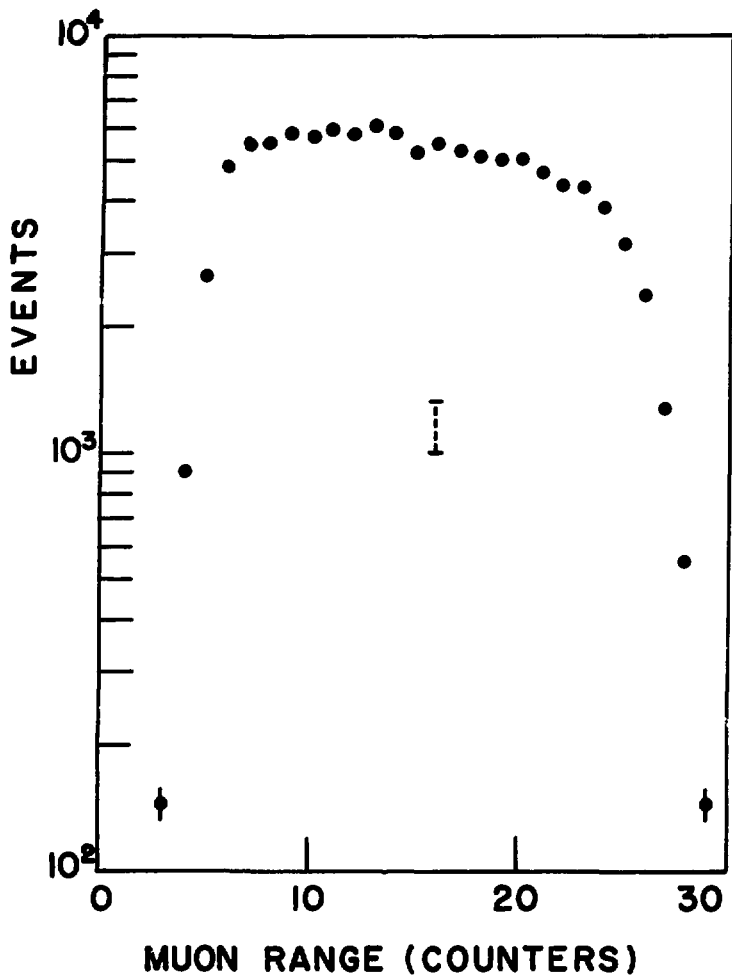


Fig. 20

XBL 759-8183